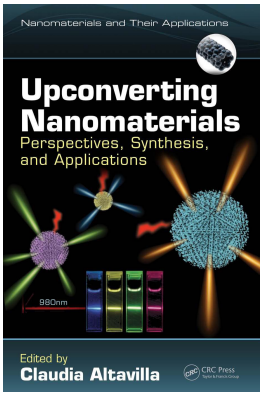

Upconverting Nanomaterials
Perspectives, Synthesis, and Applications

Claudia Altavilla

Nanothermometry Using Upconverting Nanoparticles

Publication details
https://test.routledgehandbooks.com/doi/10.1201/9781315371535-14
Eva Hemmer, Fiorenzo Vetrone
Published online on: 10 Oct 2016

11

Nanothermometry Using Upconverting Nanoparticles

Eva Hemmer and Fiorenzo Vetrone

CONTENTS

11.1 Introduction

11.1.1 Concept of Nanothermometry

Bioimaging is a vital tool in the fields of biology and medicine. For instance, it enables the study of biological processes contributing to a better

understanding of mechanisms triggering the development of diseases such as cancer. As a diagnostic tool, it is essential for the detection of diseases at a very early stage. Given the vast heterogeneity in diseases and therefore a patient's need for personalized diagnosis, the concept of multimodality is receiving increasing attention (Lee et al. 2012). In fact, multimodal imaging is a powerful tool combining the advantages of several imaging modalities while overcoming their intrinsic individual limitations. Among the most commonly applied techniques used for multimodal approaches are, for example, magnetic resonance imaging (MRI; pros: high spatial resolution, high penetration depth; cons: low sensitivity, long imaging time), computed tomography (CT; pros: high spatial resolution, high penetration depth; cons: radiation risk, not quantitative), ultrasound (US; pros: real time, low cost; cons: low resolution, operator-dependent analysis), positron emission tomography (PET; pros: high sensitivity, no penetration depth limit, quantitative, whole body scan; cons: radiation risk, high cost), single photon emission computed tomography (SPECT; pros: high sensitivity, no penetration depth limit; cons: radiation risk, low spatial resolution), and optical imaging (pros: high sensitivity, multicolor, high temporal resolution; cons: low spatial resolution, low penetration depth). This multimodal approach results in more powerful imaging tools providing increasingly reliable and accurate information, for instance increased sensitivity and higher spatial and temporal resolution when compared to single imaging modalities (Lee et al. 2012).

In recent years, it has been recognized that the temperature of a biological system is a crucial parameter that can act as a first indicator of disease or can be used to monitor biological processes. This has resulted in the emerging field of nanothermometry. Generally speaking, nanothermometry aims for the contact-less extraction of the local temperature of a given system with sub-micrometric spatial resolution (Jaque and Vetrone 2012). This is highly useful for the better understanding of processes whose dynamics and performance are dependent on the temperature of the local environment. Such thermal sensing at a well-defined local area of sub-micrometer dimensions finds specific interest in the biomedical field (Jaque et al. 2014b; Zhou et al. 2015) yet is by far not limited to biomedicine, and its rising attraction has also been reported in other fields such as micro/nanoelectronics, integrated photonics, and for the investigation of temperature and heat transfer in gaseous flows (Klimov et al. 2015; Mecklenburg et al. 2015; Perpiñà et al. 2016; Rothamer and Jordan 2012).

Many optical probes have been proven as suitable candidates for nanothermometry combining imaging capabilities with the advanced feature of temperature sensing, thus providing a powerful tool for novel multimodal thermal sensing, imaging, and potential diagnostic approaches. This chapter will first provide some theoretical background for optical nanothermometers and subsequently highlight the latest developments in the field of optical nanothermometry, with special emphasis on those probes that are based on lanthanide-doped upconverting nanoparticles (UCNPs).

11.1.2 Optical Nanothermometers

Optical nanothermometry is based on the temperature dependence of the spectral features of a phosphor. In other words, optical nanothermometry takes advantage of the fact that a phosphor's luminescence (the emission of light subsequent to the external excitation resulting in the population of electronically excited states) can be influenced by the surrounding temperature. More specifically, it is the temperature governed population probability of excited states and the subsequent generation of luminescence that is exploited in optical nanothermometry. Typical spectral features and how they are influenced by the local temperature are depicted in Figure 11.1. Based on these features, several types of nanothermometry can be described (Jaque and Vetrone 2012). Consequently, the analysis of the obtained spectral features allows us to draw conclusions about a specimen's temperature; and together with spatial optical imaging locally resolved thermal mapping of a sample becomes possible.

Luminescence intensity nanothermometry (Figure 11.1a) is based on the measurement of the intensity of the emitted light. Temperature variation changes the overall number of emitted photons, thus induces changes in the emission intensity. This is due to thermal activation of luminescence quenching mechanisms and/or increase in the non-radiative decay probabilities. While the emission intensity is rather easy to measure, a potential drawback of this approach is the sensitivity of the overall luminescence intensity to

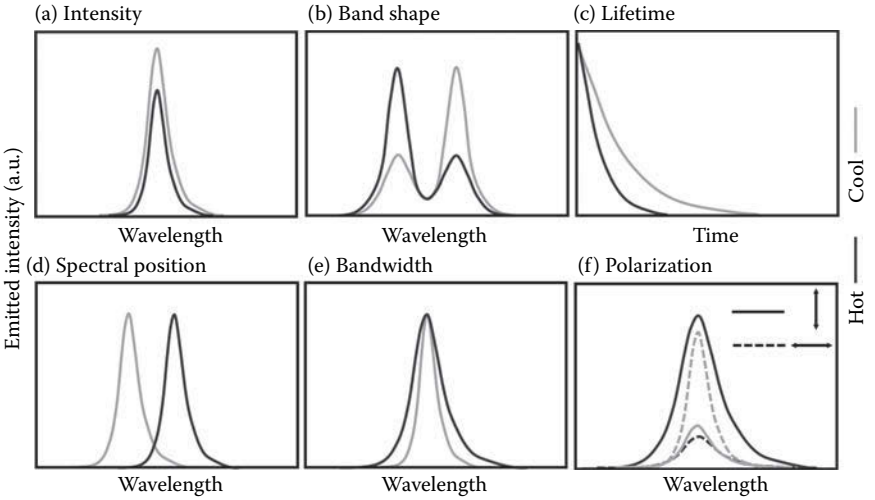

FIGURE 11.1
Schematic representation of the possible effects caused by a temperature increment on the luminescence. Dark gray lines correspond to higher temperatures. (Jaque, D. and F. Vetrone. 2012. Luminescence nanothermometry. *Nanoscale* 4:4301–26. Reproduced by permission of The Royal Society of Chemistry.)

other parameters such as probe concentration and/or the presence of other potential quenchers (e.g., in a biological sample). This makes a comparison of absolute intensities challenging. In order to overcome this, normalized spectra should be considered rather than absolute intensity values. An alternative approach is based on the analysis of intensity ratios between different spectral lines (Figure 11.1b; the herewith related luminescence intensity ratio (*LIR*) will be defined in Section 11.2.2). This type of nanothermometry, also referred to as *band-shape luminescence nanothermometry*, is most often applied with phosphors that exhibit electronic states from which emissions are generated that are very close in energy such that they are thermally coupled. Alternatively, the band shapes of two different emitters combined in one system can be used for such a ratiometric approach. The lifetime of the excited states is a further parameter that is widely employed for sensing and imaging, for instance in fluorescence lifetime microscopy (Cubeddu et al. 2002; Lakowicz et al. 1992) or in luminescence resonance energy transfer (LRET, also known as fluorescence or Förster resonance energy transfer, FRET) based assays (Mednitz and Hildebrandt 2014). *Luminescence lifetime* is defined as the time that the emitted luminescence intensity decays down to 1/e of its initial value after a pulsed excitation (assuming single exponential decay) (Wang et al. 2013). The time-dependent luminescence intensity I_t is related to the lifetime τ following Equation 11.1:

$$I_t = I_0 \cdot \exp\left(-\frac{t}{\tau}\right) \tag{11.1}$$

where I_0 is the luminescence intensity at time $t = 0$. The decay probabilities from electronic levels depend on a variety of factors, including temperature, which allows the use of lifetime data for thermal sensing (Figure 11.1c). Advantages of lifetime data over emission intensity data include their independence from phosphor concentrations and their potential for self-referencing. On the other hand, more complex read-out systems are required when compared to intensity measurements, and complications may occur when the decay profiles are not single-exponential. Further types of nanothermometry include *spectral luminescence nanothermometry* (Figure 11.1d) based on the temperature induced change of the spectral position of the emission lines; *bandwidth luminescence nanothermometry* (Figure 11.1e) exploiting line broadening upon temperature increase; and *polarization luminescence nanothermometry* (Figure 11.1f) based on the influence of the temperature on the polarization anisotropy (ratio between the luminescence intensities emitted at two orthogonal polarization states).

Thus, there are a variety of spectral features suitable for use in thermal sensing. Accordingly, remarkable phosphors and probe materials of large diversity were reported for optical thermal sensing. With regards to thermal sensing in, for example, biological systems or micro- and nanoelectronics, sub-micron size probes are required, leading to the development of

nanothermometers based on organic dyes, quantum dots, and lanthanide ions (Ln^{3+}) (Brites et al. 2011, 2012; Jaque and Vetrone 2012; Jaque et al. 2014b; Quintanilla et al. 2016; Wang et al. 2013, X. Wang et al. 2015). Wang et al. (2002) reported for the first time the use of Eu^{3+} ions for lanthanide-based nanothermometry. Since then, worldwide research efforts have led to the development of nanothermometers exploiting various Ln^{3+} ions, among them Ln^{3+}-doped UCNPs that are recently emerging as truly exciting players in the field of thermal sensing and which will be described in more detail in the following sections.

11.2 Lanthanide-Based UCNPs for Nanothermometry

11.2.1 Lanthanide-Based Upconversion

The outstanding optical properties of the lanthanides are based on the involvement of the 4*f* orbital in the electronic configuration of the trivalent lanthanide ions (Ln^{3+}), which is characterized by an incompletely filled 4*f* shell, located inside the complete $5s^2$ and $5p^6$ shells. This results in a shielding of valence electrons, which are therefore only weakly affected by the environment. Consequently, when doped in appropriate host materials, the influence of the host lattice on the optical transitions within the 4*f* configuration is small, and narrow optical absorption and emission bands as well as long lifetimes of the excited electronic states of the Ln^{3+} are obtained. Due to the electromagnetic range of the energy levels of the Ln^{3+} ions (energy diagrams of selected Ln^{3+} relevant for upconversion-based nanothermometry are shown in Figure 11.2; for a complete overview, the reader is referred to the so-called *Dieke's Diagram* [Blasse and Grabmaier 1994; Dieke 1968; Wegh et al. 2000]), Ln^{3+}-doped inorganic host materials find application as phosphors covering the broad range from laser technologies and optical communication to the biomedical field and solar applications (Barnes 2004; Y. S. Liu et al. 2013; Wang et al. 2011; W. F. Yang et al. 2014; Zagumennyi et al. 2004).

One of the characteristic features of Ln^{3+}-doped host materials is the so-called upconversion process resulting in the emission of higher energy light upon excitation with light at lower energies (Auzel 2004). While several mechanisms (energy transfer upconversion, excited-state absorption [ESA], and photon avalanche) are possible to achieve upconversion, the one most often applied is based on energy transfer between Ln^{3+} ions. This typically involves doping of an inorganic host material with activator ions, such as erbium (Er^{3+}), thulium (Tm^{3+}), holmium (Ho^{3+}) or neodymium (Nd^{3+}), and sensitizer ions (e.g., Yb^{3+}) as for example depicted in Figure 11.2.

Upon excitation of Yb^{3+} ions with near-infrared light (NIR) (980 nm) from the $^2F_{7/2}$ ground state to the sole excited state ($^2F_{5/2}$), energy transfer to the

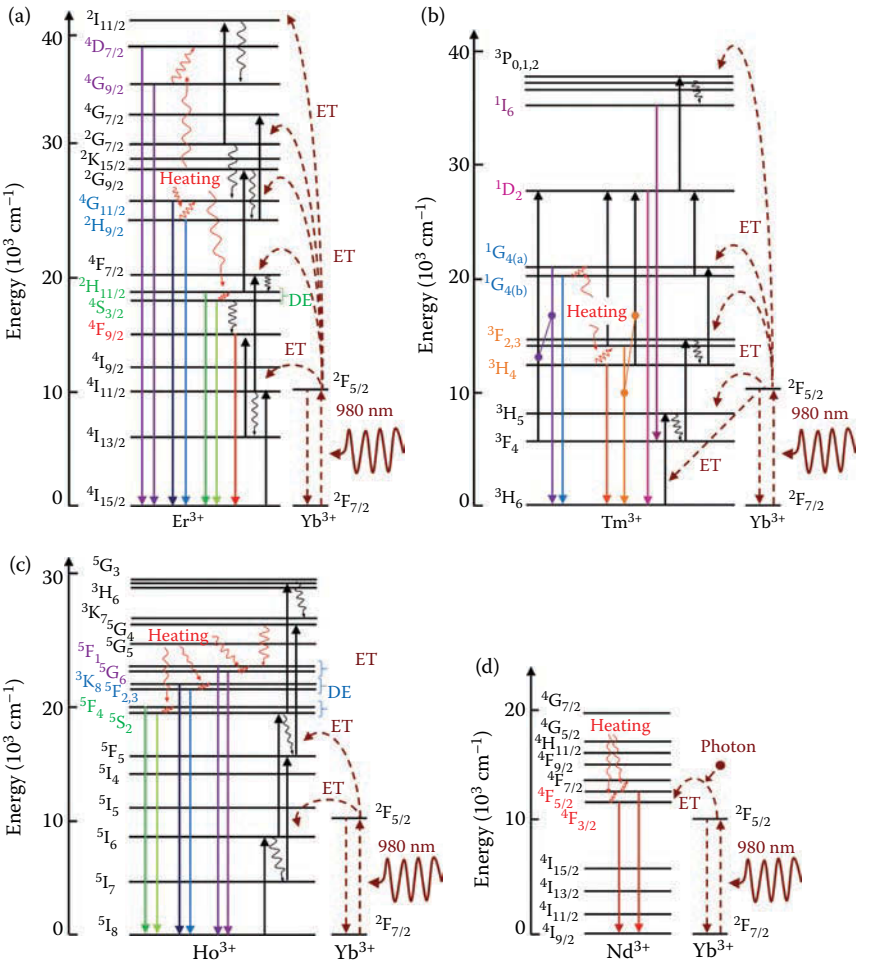

FIGURE 11.2
Mechanisms of optical thermal sensing through (a) Er^{3+}/Yb^{3+}, (b) Tm^{3+}/Yb^{3+}, (c) Ho^{3+}/Yb^{3+}, and (d) Nd^{3+}/Yb^{3+} energy transfer under 980 nm NIR excitation. "Heating" refers to the temperature increase necessary to induce the population of the higher energy levels. (Redrawn based on references Wang, R. et al. 2015. *Opt. Mater.* 43:18–24; Xu, W., Z. G. Zhang, and W. W. Cao. 2012b. *Opt. Lett.* 37:4865–67; Zheng, K. Z. et al. 2015. *Opt. Express* 23:7653–58; Quintanilla, M. et al. 2015. *J. Mater. Chem. C* 3:3108–13.)

activator ions in close proximity takes place; in case of the very well-studied Er^{3+}/Yb^{3+} system (Figure 11.2a) to the first intermediate excited state of Er^{3+}, $^4I_{11/2}$, which is resonant with the $^2F_{5/2}$ Yb^{3+} excited state. Subsequently, a second energy transfer from another Yb^{3+} ion is used for the excitation of the Ln^{3+} ions to the upper excited states (e.g., $^4F_{7/2}$ in case of Er^{3+}). This is followed by the non-radiative decay (multiphonon relaxation) to lower excited energy states (e.g., $^2H_{11/2}$ and $^4S_{3/2}$ green emitting states or $^4F_{9/2}$ red emitting state in

case of Er^{3+}) from where radiative decay to the ground state occurs resulting in the emission of light of higher energy than used for excitation. It has to be taken into account that not all cases of energy transfer upconversion are characterized by a perfect match between the excited states of the sensitizer and the activator ions. For instance in case of Tm^{3+}, Ho^{3+} or Nd^{3+} (Figure 11.2b, d), energy transfer still takes place, however, small additional amounts of energy must be provided by or be released to the host lattice in the form of phonons.

Most interestingly, the population probability of some of the excited energy states is highly sensitive to temperature changes in the local environment of the Ln^{3+} ions (Figure 11.2). This allows for the exploitation of upconverting materials as optical nanothermometers, specifically as ratiometric nanothermometers. Further insight into the theoretical background of these temperature controlled processes will be provided in the following section.

11.2.2 Theoretical Background: *LIR*, Boltzmann's Plot, Thermal Sensitivity, and Thermal Resolution

As previously mentioned, the use of ratiometric nanothermometers exploiting the thermally induced variation of more than one emission intensity is a suitable tool to overcome drawbacks of techniques relying solely on one emission intensity. Seeking highly reliable intensity ratios, the *LIR* technique provides an attractive alternative tool (Quintanilla et al. 2011; Vetrone et al. 2010). This technique is based on the intensity ratio between two closely spaced energy levels that are thermally coupled. Generally, the energy gap between the two levels must be small, typically smaller than ~2000 cm^{-1}, in order to allow thermal coupling. The temperature governed population of the upper of the two levels involved is then described by Boltzmann's distribution. Under such conditions, *LIR* can be defined by Equation 11.2 (Quintanilla et al. 2011):

$$LIR = \frac{I_1}{I_2} = B \cdot \exp\left(-\frac{\Delta E}{k_B \cdot T}\right) \tag{11.2}$$

where ΔE is the energy gap between the emitting levels in close proximity I_1 (upper level) and I_2 (lower level). Temperature T is given in Kelvin. k_B is the Boltzmann factor. B is a constant that depends on the experimental system and the intrinsic spectroscopic parameters of the dopant/host pair (Equation 11.3):

$$B = \frac{c_1(v) \cdot A_1 \cdot g_1 \cdot h \cdot v_1}{c_2(v) \cdot A_2 \cdot g_2 \cdot h \cdot v_2} \tag{11.3}$$

where h is the Plank's constant, $A_{1,2}$ is the spontaneous emission rate of the level, $g_{1,2}$ its degeneracy, and $c_{1,2}(v)$ is the response of the detection system at

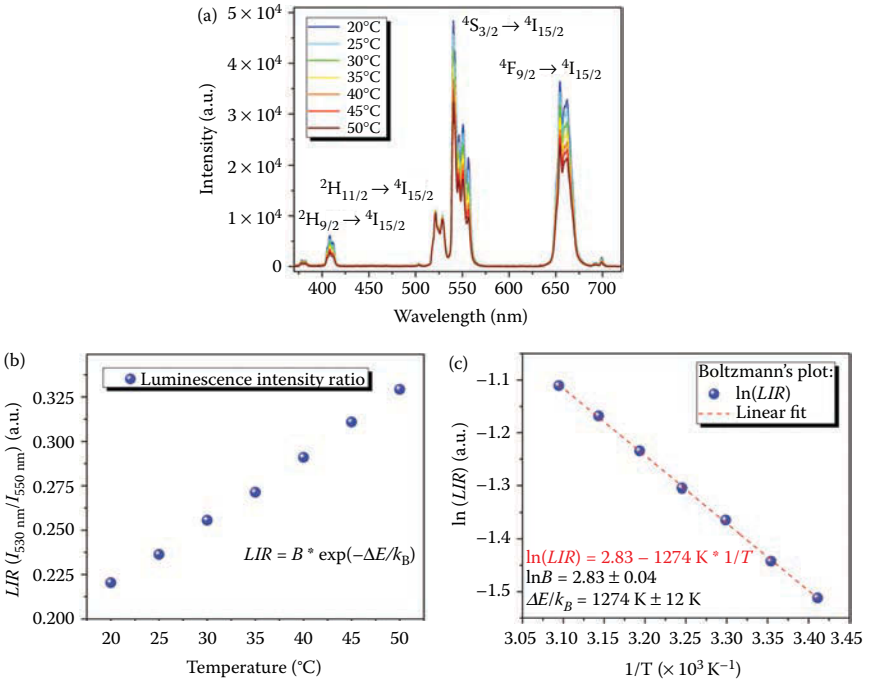

FIGURE 11.3
(a) Typical temperature dependent upconversion emission spectra of Er^{3+}/Yb^{3+} co-doped UCNPs (β-$NaGdF_4$ doped with 2 mol% Er^{3+} and 20 mol% Yb^{3+}; dispersed in H_2O; particle size: ~26 nm; excitation with a 980 nm laser diode; laser power: 330 mW). (b) *LIR* as a function of the temperature. (c) Boltzmann's plot. (Data taken from Hemmer, E. et al. 2015. *Chem. Mater.* 27:235–44.)

the emission frequency $v_{1,2}$. ΔE and B can be obtained from the least-squares fitting of the linear dependence of ln(*LIR*) versus the reciprocal absolute temperature, $1/T$, so-called Boltzmann's plot (Equation 11.4, Figure 11.3).

$$\ln(LIR) = \ln(B) - \frac{\Delta E}{k_B \cdot T} \tag{11.4}$$

The green emitting states $^2H_{11/2}$ and $^4S_{3/2}$ of Er^{3+} are among the most widely exploited energy levels for *LIR*-based nanothermometry with lanthanides (Figure 11.2a, Figure 11.3 and Section 11.3.1). By far less exploited is the use of Er^{3+}-based short-wavelength upconversion emission for thermal sensing. Xu et al. (2012b) verified the thermal coupling between the $^4G_{11/2}$ (384 nm) and $^2H_{9/2}$ (408 nm) excited states in Er^{3+}/Yb^{3+} co-doped $CaWO_4$, resulting in the shortest wavelength emissions for optical temperature measurement at the time. The well-separated emissions in the ultraviolet (UV) region at

384 and 408 nm (following a three-photon excitation process) are specifically favorable for high-temperature thermal sensing since the interference of background radiation can be avoided. Zheng et al. (2015) demonstrated that the $^4D_{7/2}$ (256 nm) and $^4G_{9/2}$ (276 nm) excited states of Er^{3+} ions doped into β-$NaLuF_4$ nanocrystals are thermally coupled and that their population ratio is fitted well by the Boltzmann's distribution. It was further shown that the thermal sensitivity of the five-photon upconversion emission in the UV region was superior to that of the green-based ratiometric nanothermometer ($^2H_{11/2}$: $^4S_{3/2}$) from room temperature to 330 K.

Moreover, the *LIR* technique is not limited to Er^{3+}-based UCNPs. Other (upconverting) Ln^{3+} ions possessing energy levels in close proximity whose thermal population is governed by Boltzmann's distribution include Tm^{3+}, Ho^{3+}, and Nd^{3+} (Figure 11.2b–d). Most recent research achievements involving these systems in nanothermometry will be highlighted in Section 11.3. Moreover, it must be noted that the *LIR* approach cannot only be applied between intensities originating from two emitting electronic levels separated by a small energy gap, but also to intensities that result from one emitting level if that specific level shows well-separated Stark sub-levels. For instance, the thermally coupled sub-Stark energy levels of the $^4F_{9/2}$ level in Er^{3+}, the $^3H_4$ excited state of the Tm^{3+} ions, or the high- and low-energy Stark sub-levels of the $^4F_{3/2}$ state of the Nd^{3+} ions (Dong et al. 2011; Liu et al. 2011; Rocha et al. 2014).

In order to describe the performance and suitability of a probe material as an optical temperature sensor, it is further necessary to introduce a measure to express the extent to which a thermally sensitive parameter changes upon temperature fluctuation, which is the *thermal sensitivity*, *S*. In this context, the *LIR* technique is a suitable tool to determine the thermal sensitivity of an Ln^{3+}-based nanothermometer, as it is defined by (Quintanilla et al. 2011)

$$S = \frac{\partial(LIR)}{\partial T} = LIR \cdot \left(\frac{\Delta E}{k_B \cdot T^2} \right) \tag{11.5}$$

where $LIR = I_1/I_2$ is determined by integration of the emission peaks and $\Delta E/k_B$ is given by the Boltzmann's plot (Figure 11.3c).

However, it must be taken into account that Equation 11.5 can only be applied if the population of the energy levels involved is Boltzmann governed. For instance in the case of surface functionalization or combination of UCNPs with additional energy acceptors or donors (such as organic dyes or quantum dots), partial quenching of the emission from the UCNPs can occur, and one cannot assume any longer Boltzmann's distribution between the energy levels. Under such conditions, it is still possible to estimate *S* by applying the basic definition of *S* as the thermal derivative of the *LIR*. However, a function different from the one given in Equation 11.5 for *LIR* has to be determined based on the experimental data for the ratio between the two intensities involved. This is possible by fitting the experimental *LIR*

data, and the obtained fitted function, more precisely its thermal derivative, can then be applied in order to estimate the sensitivity of the system. (Hemmer et al. 2015). A further aspect that needs to be considered when estimating the sensitivity of an optical nanothermometer is optical heating. As shown by Rakov and Maciel (2012) continuous wave (cw) laser excitation of a probe at a given external temperature (i.e., the temperature at which the overall sample is kept by external heating/cooling) induces internal probe heating dependent on the applied laser power. This internal heating reduced the sensitivity of the thermal sensor. It was observed, however, that the use of pulsed excitation eliminated the optical heating effect and the maximum sensitivity of the investigated sensor increased from ~0.0056 K^{-1} for cw to ~0.0070 K^{-1} for pulsed excitation.

Finally, while the thermal sensitivity is a suitable parameter to describe the performance of a nanothermometer that enables the comparison of various systems (Figure 11.4 displays *S* of various upconverting materials [Quintanilla et al. 2016]), it has to be kept in mind that it does not take into account signal-to-noise-ratios or different emission quantum yields of different probes. However, these are essential experimental aspects and their consideration becomes necessary in terms of practical application. Therefore, an additional parameter has to be introduced to further describe the performance of an optical nanothermometer, namely the *thermal resolution*, ΔT_{min}.

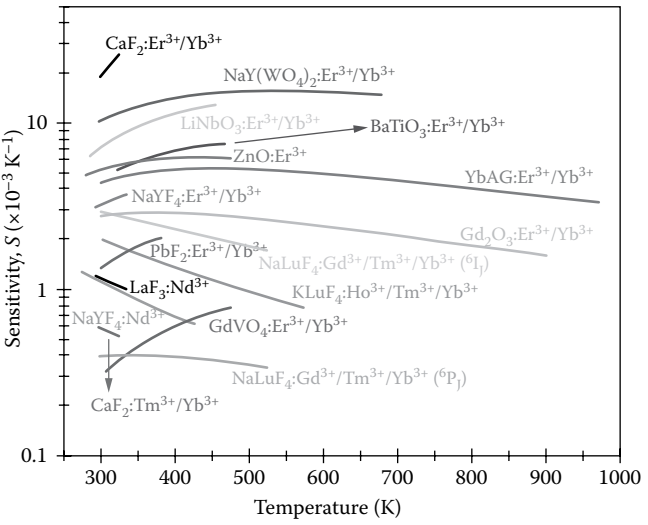

FIGURE 11.4
Thermal sensitivities of different upconverting materials proposed for *LIR*-based nanothermometry. (Quintanilla, M. et al. 2016. Luminescent nanothermometry with lanthanide-doped nanoparticles. In *Thermometry at the Nanoscale: Techniques and Selected Applications*, edited by L. D. Carlos, and F. Palacio, 124–66. Cambridge: The Royal Society of Chemistry. Reproduced by permission of Royal Society of Chemistry.)

The thermal resolution is defined as the minimum temperature that can be effectively resolved, and it can be statistically described for a given temperature by

$$\Delta T = \frac{\sigma}{S} \tag{11.6}$$

where σ is the standard derivation of several measurements and S is the sensitivity at this temperature (Quintanilla et al. 2016).

11.3 Recent Advances in UCNP-Based Nanothermometry

11.3.1 Er^{3+}-Based Nanothermometers

The dopant pair Er^{3+}/Yb^{3+} is one of the most intensively studied systems with regards to upconverting materials, and temperature dependent Er^{3+}/Yb^{3+}-based upconversion was reported for very diverse host materials, for instance, ceramics (F. Huang et al. 2015; Peng et al. 2012; Y. Yang et al. 2014; Y. M. Yang et al. 2014; Zou et al. 2015), glasses (dos Santos et al. 1999; Lai et al. 2010; Pandey et al. 2014), fluoride-based crystals (Chouahda et al. 2009; Jaque and Vetrone 2012; Sayoud et al. 2012; Vetrone et al. 2010), or composite materials such as UCNPs embedded in a glass matrix (Chen et al. 2015; Jiang et al. 2014).

Based on their studies of Er^{3+}/Yb^{3+}-doped Gd_2O_3, Singh et al. (2009) summarized the advantages of nanocrystalline host materials, namely their advanced thermal stability allowing for high-temperature sensing, and their chemical stability making this type of temperature sensor a permanent and robust device. Following this idea, low- and high-temperature sensing covering the broad region from 93 to 613 K was demonstrated for Y_2O_3:Er^{3+}/Yb^{3+} revealing its suitability as a thermal sensor for a very broad temperature range (Du et al. 2015b). Another example for recent achievements in the development of upconversion-based nanothermometers is the work by Gavrilovic et al. (2014) reporting a high relative sensitivity of 1.11% K^{-1} with an estimated thermal resolution of 1 K for Er^{3+}/Yb^{3+} co-doped $GdVO_4$UCNPs.

When developing optical thermal sensors, it is the obvious goal to achieve optimized thermal sensitivity. In this context, several parameters have been identified that play a key role for the design of high-performing thermal probes, including characteristics of (i) the host lattice (e.g., phonon energy, lattice distortions, and crystal field), (ii) the dopant ions (e.g., Ln^{3+} concentration, use of co-dopants), (iii) the particle morphology (size and shape), and (iv) the local probe environment (e.g., solvent, surface modification, and core–shell structures).

Regarding the host lattice, it was shown that annealing at higher temperatures affects the energy gap between the $^2H_{11/2}$ and $^4S_{3/2}$ levels of Er^{3+} ions doped into a ZnO matrix, resulting in a larger energy gap and a less efficient population of the $^2H_{11/2}$ level by thermalization when the probe was annealed (Wang et al. 2007). In general, the energy levels of Ln^{3+} ions in a solid host material experience Stark splitting, which occurs as the degenerate 4*f* levels are further split in the crystal field as a result of the local atomic configuration around the Ln^{3+} ions. Further, the degree of this Stark splitting influences the energy gap between two levels in close proximity (such as $^2H_{11/2}$ and $^4S_{3/2}$ in Er^{3+}). Thus, when annealing ZnO:Er^{3+} at high temperature, the local atomic configuration around the optically active Er^{3+} ions was modified leading to a variation of the crystal field around the Er^{3+} ions and a change of the energy gap between the two energy levels. In a different study, L. Liu et al. (2013) suggested that the larger energy gap between the $^2H_{11/2}$ and $^4S_{3/2}$ levels of Er^{3+} in Y_2O_3 nanoparticles is due to the alteration of Er^{3+} clusters in the Y_2O_3 matrix after applying a re-crystallization procedure on the Y_2O_3:Er^{3+} probe.

Further, seeking enhanced upconversion emission, the lattice phonon energy of the host material is an important factor. Since it strongly affects the upconversion emission, it is also expected to alter the sensitivity of a thermal sensor. In this context, Singh et al. (2015) investigated the optical and structural properties of three different probe materials, namely Er^{3+}/Yb^{3+} co-doped yttrium oxide (cubic $Y_{1.894}Yb_{0.1}Er_{0.006}O_3$), yttrium vanadate (tetragonal $Y_{0.947}Yb_{0.05}Er_{0.003}VO_4$), and yttrium phosphate ($Y_{0.947}Yb_{0.05}Er_{0.003}PO_4$). It was found that the thermal sensitivity and the *LIR* of the phosphate probe was significantly lower than that of the two other probes, most likely due to the higher phonon energy of the phosphate host lattice, enhancing non-radiative relaxation from the $^2H_{11/2}$ to the $^4S_{3/2}$ level, resulting in the increase of the $^4S_{3/2}$ originating emission when compared to the $^2H_{11/2}$ emission. Moreover, the authors report the vanadate-based phosphor $Y_{0.947}Yb_{0.05}Er_{0.003}VO_4$ as the *LIR*-based thermal sensor with the highest sensitivity (0.0105 K^{-1}) to date. Further work investigating the influence of the host lattice on the sensing performance was conducted by Liu et al. (2015) focusing on Yb^{3+}-sensitized Er^{3+}-doped Y_2O_3, YAG, and $LaAlO_3$ phosphors. It was found that the thermal sensitivity of the phosphors was proportional to the bond covalency of Y-O and La-O calculated following bond theory. These results highlight the importance of better understanding of the probes' structural and optical properties for the rational design of novel Ln-based nanothermometers.

Besides the host lattice, dopant concentration shows an effect on temperature sensing behavior. For instance, an increase in the maximal thermal sensitivity of Er^{3+}-doped Y_2O_3 from about 0.0028 K^{-1} to 0.0052 K^{-1} (at 741 K) was observed when the Er^{3+} doping concentration decreased from 12 mol% to lower doing concentration (0.5 and 1 mol%) (R. Wang et al. 2015). Since the energy gaps obtained from the Boltzmann's plots were substantially identical (1053 and 1030 cm^{-1}), the enhanced sensitivity must come from the parameter *B* in Equation 11.2. It was further shown that the larger *B* is attributed

to a larger ratio of the spontaneous emission rates A_1/A_2 (Equation 11.3) in weakly doped samples. This is due to the fact that high doping concentrations can induce structural changes in the crystal lattice of the host material. In fact, these changes are expressed in the decrease of the cell parameters of the crystalline Y_2O_3 host lattice from 10.6035 Å to 10.5975 Å with the doping concentration increasing from 0.5 to 12 mol%. In general, the Ln^{3+} dopant ions replace stoichiometrically the metal ions in the host lattice, and changes of the host's crystal lattice are induced due to the differences in the ionic sizes of the dopant and the host ions. Eventually, these local structural changes affect the spontaneous emission rates, which are known to be very sensitive to the Ln^{3+} surrounding environment. In the same study, similar results were reported for Er^{3+}/Yb^{3+} co-doped $NaYF_4$.

Besides the concentration of the activator Ln^{3+} ion, co-doping of other ions into the host lattice has an effect on the Er^{3+}/Yb^{3+} upconversion emission and the performance of the resultant probe material as a thermal sensor. For instance, a set of studies discusses the effect of molybdenum (Mo) as co-dopant on the upconversion efficiency and the optical temperature sensing behavior, including Er/Mo:Yb_2TiO_7 (Cao et al. 2011), Er/Yb/Mo:$Na_{0.5}Bi_{0.5}TiO_3$, (Du and Yu 2015) Yb^{3+}/Er^{3+}:$AgLa(MoO_4)_2$, (Li et al. 2015) Er^{3+}/Yb^{3+}:$NaY(MoO_4)_2$ (Yang et al. 2015), or Er/Mo:$Yb_3Al_5O_{12}$ (Dong et al. 2012). The significant increase of the green upconversion emission has been assigned to an energy transfer process based on ground state absorption (GSA) and subsequent ESA in a Yb^{3+}–MnO_4^{2-} dimer complex, followed by a high excited-state energy transfer to the Er^{3+} ions. Moreover, it has to be noted that the temperature sensing properties of the Er^{3+}/Yb^{3+} ions in the described ceramic host materials were found to be enhanced by co-doping with Mo ions. As a further example showing the strong effect co-doping can have on the upconversion luminescence properties, Klier and Kumke (2015a) analyzed $NaYF_4$:Er^{3+}/Yb^{3+} co-doped with Gd^{3+} and revealed not only a strong dependence of the emission intensity distribution (e.g., green–red ratio) on the Gd^{3+} content, but also—most interesting with regard to nanothermometry—on the temperature profile of the luminescence intensity.

With regard to the influence of the probes' morphology on their thermal sensing performance, Dong et al. (2014) observed an increase of the thermal sensitivity when decreasing the size of Er^{3+}/Yb^{3+}:$NaYF_4$ upconverting microspheres from 1.6 to 0.7 μm (S(1.6 μm) = 24.7 · 10^{-4} K^{-1}; S(0.7 μm) = 36.8 · 10^{-4} K^{-1}). The size-dependent sensitivity to T was assigned to the increased surface to volume ratio for smaller spheres resulting in more Er^{3+} ions in close proximity to the sphere surface. Generally speaking, Ln^{3+} ions located at the surface of a particle undergo stronger electron–phonon interactions with changing temperature than the Ln^{3+} ions located inside. Consequently, in the case of the Er^{3+} doped into smaller spheres, the population process of $^4S_{3/2} \rightarrow {}^2H_{11/2}$ increases and the effect of the *LIR* ($I(^2H_{11/2})/I(^4S_{3/2})$) is enhanced. It must also be taken into account that undesired optical heating by the NIR excitation laser is more pronounced in smaller nano/microparticles than in larger ones, which results

from the higher efficiency of a non-radiative relaxation process and enhanced electron–phonon interaction in nano/microparticles. Studies by Maciel et al. (2010) on Er^{3+}-doped $BaTiO_3$ UCNPs (26 and 58 nm in size) further confirmed the size dependence of the thermal sensing performance, while the sensitivity was found to be independent from the surrounding medium (comparing air, water, and glycerol).

Among upconverting nanomaterials, β-$NaYF_4$:Er^{3+}/Yb^{3+} UCNPs are commonly considered as one of the most efficient upconverting nanomaterials. However, their upconversion efficiency is still low (typically below 1 %) and efforts are undertaken for improvement. Upconversion efficiency enhancement is, for example, obtained by designing a core–shell structure where the Ln^{3+} ions are doped in the core and are well protected from the environment by an undoped shell. Vetrone et al. (2009) showed that the use of an active shell, doped with Yb^{3+}, allows for further upconversion enhancement. Since then, the concept of core–shell UCNPs has widely been applied. Nevertheless, the influence of a core–shell design on the thermal sensitivity of UCNPs has received much less attention. Li et al. (2014) compared the thermal behavior of core only, core-inert (undoped $NaYF_4$) shell, as well as core-active ($NaYF_4$:10% Yb^{3+}) shell β-$NaYF_4$:Er^{3+}/Yb^{3+} UCNPs. As expected, the inert and active shells significantly enhance the upconversion intensity of the UCNPs. Of special interest for application of these UCNPs as nanothermometers is the finding that the core–shell design does not alter their sensitivity to *T*. Importantly, it was found that the use of an active shell results in similar optical heating effect as in case of core only UCNPs. However, such undesired heating is almost negligible when an inert shell is applied, which can be attributed to the lack of NIR excitation light absorbing Yb^{3+} ions in the shell and the subsequent conversion of parts of absorbed energy into heat. The authors further showed that thermal-sensing properties of UCNPs are not affected by different dispersion media and that UCNPs exhibit high stability in broad pH range and salt conditions. These characteristics are highly suitable for biomedical applications.

In the context of biomedical applications, specifically with regard to tumor treatment and photothermal therapy approaches, Mahata et al. (2015) reported Er^{3+}/Yb^{3+} co-doped yttrium vanadate (YVO_4) UCNPs as highly sensitive nanothermometers (0.01169 K^{-1} at 380 K, to date claimed as the highest calculated sensitivity among reported results for inorganic nanosensors) and optical nanoheaters. While optical heating has previously been described as undesired, it also opens pathways for photothermal therapeutic approaches. In fact, Mahata et al. (2015) observed a temperature increase from 315 to 460 K under excitation of the UCNPs with 920 nm light. This excessive heat generation in the sample was assigned to the involved non-radiative processes, whereas the non-radiative decay rates increase exponentially with *T*. In addition, the previously mentioned stronger electron–phonon coupling in nanocrystalline particles when compared to larger particles or bulk materials enhances the non-radiative transition, providing additional contribution to the heat generation.

It becomes clear that, since the first mention of Ln^{3+}-based nanothermometry, much effort has been undertaken for a better understanding of the thermal behavior of (Er^{3+}-based) UCNPs and the design of highly sensitive thermal probes, resulting in promising candidates for applications in nanothermometry. In the following section, some of the most recent examples of Er^{3+}-doped UCNP-based nanothermometry for biomedical applications will be highlighted.

11.3.1.1 Er^{3+}-Based Upconverting Nanothermometers for Biomedical Applications

The first intracellular nanothermometry by use of UCNPs was realized by Vetrone et al. (2010). In this work, $NaYF_4$:Er^{3+}/Yb^{3+} UCNPs were incubated with human carcinoma (HeLa) cells in order to induce the cellular uptake of the nanothermometers. Subsequently, the optical transmission image of an individual HeLa cell was obtained at different inner temperatures set by use of a resistor-based heater. Upon changing of the applied voltage, and therewith of the internal temperature of the cells, the *LIR* (I_{525}/I_{545}) of the nanothermometer changed, where I_{525} and I_{545} are the relative upconverting emissions emanating from the thermally coupled $^2H_{11/2}$ and $^4S_{3/2}$ states, respectively. With the help of a previously recorded calibration curve (Figure 11.5a and b), the internal temperature of a single HeLa cell could be assigned (Figure 11.5c) and monitored until thermally induced cell death occurred.

Jaque et al. (2013) used a similar concept in order to monitor the thermal loading induced by tightly focused laser beams in both living cells and fluids. Very interesting from a biomedical application point of view, it was found that for the typical excitation intensities used in bioimaging experiments, pump-induced optical heating could be neglected. However, for larger excitation intensities (tens of MW cm^{-2}), the local thermal loading was found to be large enough to cause cell death.

Savchuk et al. (2014) developed fluorescence lifetime nanothermometers based on Er^{3+}/Yb^{3+}:NaY_2F_5O or Er^{3+}/Yb^{3+}: $NaYF_4$ UCNPs, whereas it was demonstrated that Er^{3+}/Yb^{3+}:NaY_2F_5O possesses a higher thermal sensitivity than Er^{3+}/Yb^{3+}:$NaYF_4$. Most importantly, the first experimental evidence on sub-tissue lifetime fluorescence thermal sensing by UCNPs in an *ex vivo* experiment was provided. Therefore, subsequent to sub-tissue injection of the Er^{3+}/Yb^{3+}:NaY_2F_5O UCNPs 1 mm below the surface of a chicken breast, local optical heating was induced by use of a 1090 nm heating laser (1.2 W), followed by recording of the fluorescence decay curves (excitation of Er^{3+}/Yb^{3+} by 980 nm). It was found that the lifetime measured inside the chicken breast was substantially reduced when the heating laser was on, providing evidence for the progressive heating of the tissue.

In a different approach, Schartner and Monro (2014) demonstrated localized temperature measurement using a probe (sodium zinc tellurite glass, doped with 1 mol% Er^{3+} and 9 mol% Yb^{3+}) at the tip of an optical fiber. Since

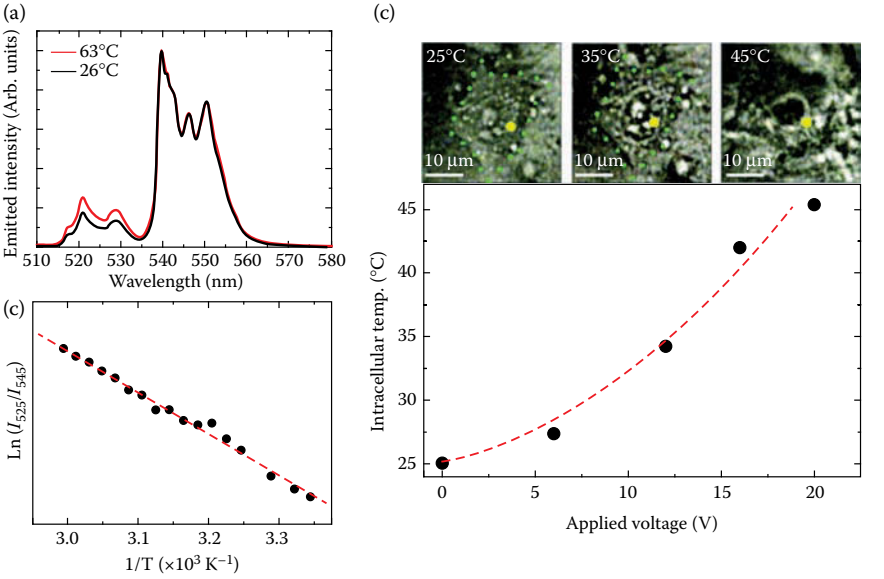

FIGURE 11.5
(a) Upconversion emission spectra obtained at two different cuvette temperatures (excitation at 920 nm) and (b) a plot of $\ln(I_{525}/I_{545})$ as a function of $1/T$ to calibrate the thermometric scale for the water-dispersible $NaYF_4:Er^{3+}/Yb^{3+}$ nanothermometers. (c) (Top) Optical transmission images of an individual HeLa cell at three inner temperatures. Cell death is observed at 45°C. (Bottom) Temperature of the HeLa cell determined by the Er^{3+} ion fluorescence in the $NaYF_4:Er^{3+}/Yb^{3+}$ UCNPs as a function of the applied voltage. (Reprinted with permission from Vetrone, F. et al. 2010. Temperature sensing using fluorescent nanothermometers. *ACS Nano* 4, 3254–58. Copyright 2010 American Chemical Society.)

the tip of a typical fiber is only 125 µm in size, this probe shows, for instance, potential for *in vivo* applications; namely thermal sensing of deeper tissue areas that are difficult to access and where the limited tissue penetration depth of visible light needs to be overcome. The point temperature sensing device exhibits a temperature resolution of approximately 0.1–0.3°C over the biological relevant range from 23°C to 39°C. Moreover, the application of a relatively thin probe layer with a high dopant concentration allowed to minimize the required excitation power to 300 µW (98 mW mm^{-2}), reducing the potential for heat induced damage to biological samples.

11.3.2 Tm^{3+}-Based Nanothermometers

As depicted in Figure 11.2b, Tm^{3+} ions show potential for upconversion-based thermal sensing based on the thermal coupling of their excited states such as $^3F_{2,3}$ and $^3H_4$. Taking advantage of this, Xing et al. (2014) proposed Tm^{3+}/Yb^{3+} co-doped $LiNbO_3$ single crystals as a highly sensitive optical temperature sensor based on the *LIR* technique. Due to the thermal population of the

$^3F_{2,3}$ level from the $^3H_4$ level, the emission intensity at 700 nm ($^3F_{2,3} \rightarrow {}^3H_6$) is greatly enhanced with increasing temperature, while the emission intensity at 800 nm ($^3H_4 \rightarrow {}^3H_6$) decreases.

Further, Tm^{3+} exhibits two distinct blue upconversion emission peaks at 477 and 488 nm that are assigned to the transition from the Stark sub-levels of the $^1G_4$ state to the $^3H_6$ ground state of Tm^{3+} ions. Variation of temperature causes a relevant change in the intensity ratio of these two luminescence lines. Exploiting the temperature induced population redistribution between these Stark levels of the $^1G_4$ state of Tm^{3+}, nanothermometry by use of, for example, Tm^{3+}/Yb^{3+}co-doped $NaNbO_3$ (Pereira et al. 2015) or $Na_2Y_2B_2O_7$ (Soni et al. 2015) nanoprobes has recently been reported.

Aside from the use of thermally coupled energy levels in close proximity to each other or of Stark sub-levels, an approach based on the thermally controlled population of energy levels in further distance was suggested by Zhou et al. (2014a) who designed a core–shell structure based on a Tm^{3+}/Yb^{3+} co-doped $NaYF_4$ core and a Pr^{3+}-doped $NaYF_4$ shell (Figure 11.6a).

The resultant core–shell UCNPs allowed for the exploitation of the temperature dependent population of different Tm^{3+} energy levels for nanothermometry, while the Pr^{3+}-doped shell was used to evaluate potential optical heating effects. Pr^{3+}-doped host materials are known for their thermally coupled energy levels, $^3P_2$ and $^3P_0$ suitable for *LIR*-based thermal sensing upon direct excitation with a blue laser (no upconversion process) (Zhou et al. 2014b). Importantly, there is no evidence for optical heating upon such direct excitation, which allows us to use the temperature dependent emission of Pr^{3+} ions to detect a potential heating of the core–shell structure caused by illumination with the 980 nm laser required for the excitation of Tm^{3+}/Yb^{3+} ions. Simultaneous excitation of the sample with 447 and 980 nm lasers revealed that optical heating can be neglected up to a laser power of 47 mW (spot size of the irradiated area: 2 mm × 3 mm). Subsequently, the different thermal behavior of the two upconversion emissions at 696 and 646 nm originating from the $^3F_{2,3}$ and $^1G_4$ excited states of Tm^{3+} ions were used for thermal sensing upon 980 nm excitation (Figure 11.6b). It was shown that the 696 nm emission ($^3F_{2,3} \rightarrow {}^3H_6$) increases monotonously with T due to the thermal population of the $^3F_{2,3}$ states from the lower $^3H_4$ state (Figure 11.6c). In contrast, the 646 nm emission ($^1G_4 \rightarrow {}^3F_4$) first increases with increasing temperature until 390 K, followed by a decrease. This behavior was explained as follows. Due to the energy mismatch between the Yb^{3+} and Tm^{3+} ions, the upconverted population of the $^1G_4$ level is sensitive to the participation of phonons, fostering the level's population when the temperature increases. However, phonon-assisted cross relaxation may be triggered by further temperature increase resulting in a decreasing $^1G_4$ population and consequently reduced emission intensity. Moreover, the $^1G_4$ state is populated from the $^3H_4$ state by an energy transfer process. A decreased $^3H_4$ population caused by thermal population of the $^3F_{2,3}$ levels will therefore further reduce the population of the $^1G_4$ level. Thus, it is a complex interplay between different phonon-assisted processes governing

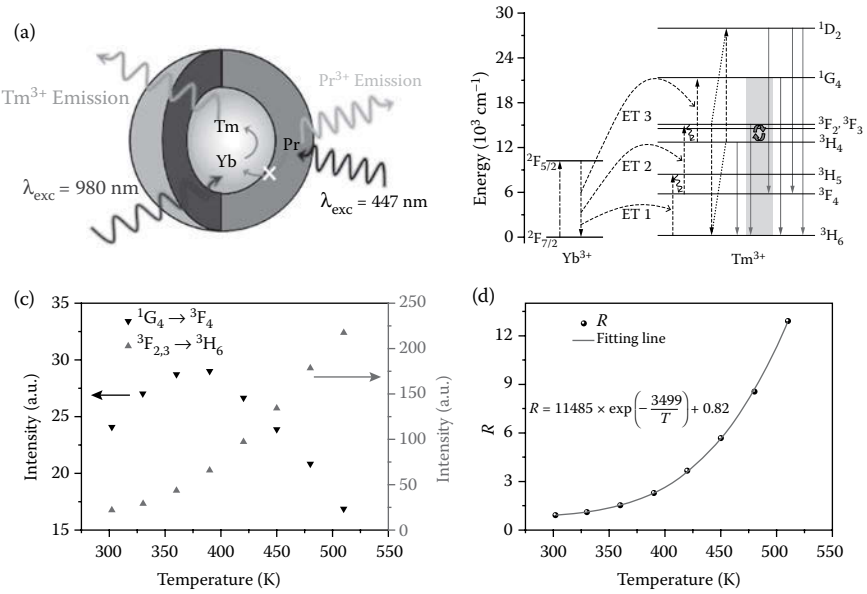

FIGURE 11.6
(a) Schematic diagram of the Tm^{3+}/Yb^{3+}:$NaYF_4$ core/Pr^{3+}:$NaYF_4$ shell UCNPs. (b) Schematic illustration of the upconversion processes in the UCNPs under 980 nm excitation. The dashed-dotted, dashed, curved, and full arrows indicate photon excitation, energy transfer, multiphonon relaxation, and emission processes. (c) Integral emission intensities of $^3F_{2,3} \rightarrow {}^3H_6$ and $^1G_4 \rightarrow {}^3F_4$ transitions as a function of *T*. (d) *T* dependence of the ratio R (*LIR*) between these integral intensities. (Reproduced from Zhou, S.S. et al. 2014. *Opt. Lett.*, 39: 6687–90, with permission of The Optical Society.)

the population of the different Tm^{3+} energy levels, eventually resulting in the highly temperature sensitive emission from two not directly thermally coupled energy levels (Figure 11.6d: *LIR* as a function of *T*).

Aiming for photodynamic therapy (Bhaumik et al. 2015; Idris et al. 2015), for example for the treatment of skin cancer, UV-generating phosphors are highly attractive probes. However, UV light is strongly absorbed and scattered by biological tissue restricting the accessible regions when using external UV excitation sources. In contrast, absorption and scattering of NIR light by biological media is significantly reduced when compared to UV light (Anderson and Parrish 1981; Smith et al. 2009). Consequently, in order to broaden the field in which UV light can be applied, the generation of UV light under NIR light excitation was suggested. In this context, Tm^{3+}-doped UCNPs have been proven as excellent UV emitters following 980 nm laser excitation.

For example, Tm^{3+}/Yb^{3+} co-doped SrF_2 UCNPs were synthesized and their *T*-dependent emission properties were carefully analyzed by Quintanilla et al. (2015). Besides emission peaks in the visible region, Tm^{3+} shows two strong emission bands in the UV at around 370 and 350 nm, which can be assigned to the radiative transitions of the excited $^1D_2$ and $^1I_6$ levels.

The upconversion route that populates the $^1D_2$ state is often described as a combination of several energy transfer processes combining energy transfer from the $^2F_{5/2}$ Yb^{3+} excited state to Tm^{3+} ions and (due to the strong non-resonant character of this energy transfer) Tm^{3+}–Tm^{3+} cross-relaxation processes (Figure 11.2b). The population of $^1I_6$ takes place after a fifth energy transfer process from excited Yb^{3+} ions in the vicinity. Figure 11.7 shows the upconversion emission spectra obtained under 980 nm excitation and the peak intensities of the main emissions as a function of *T*.

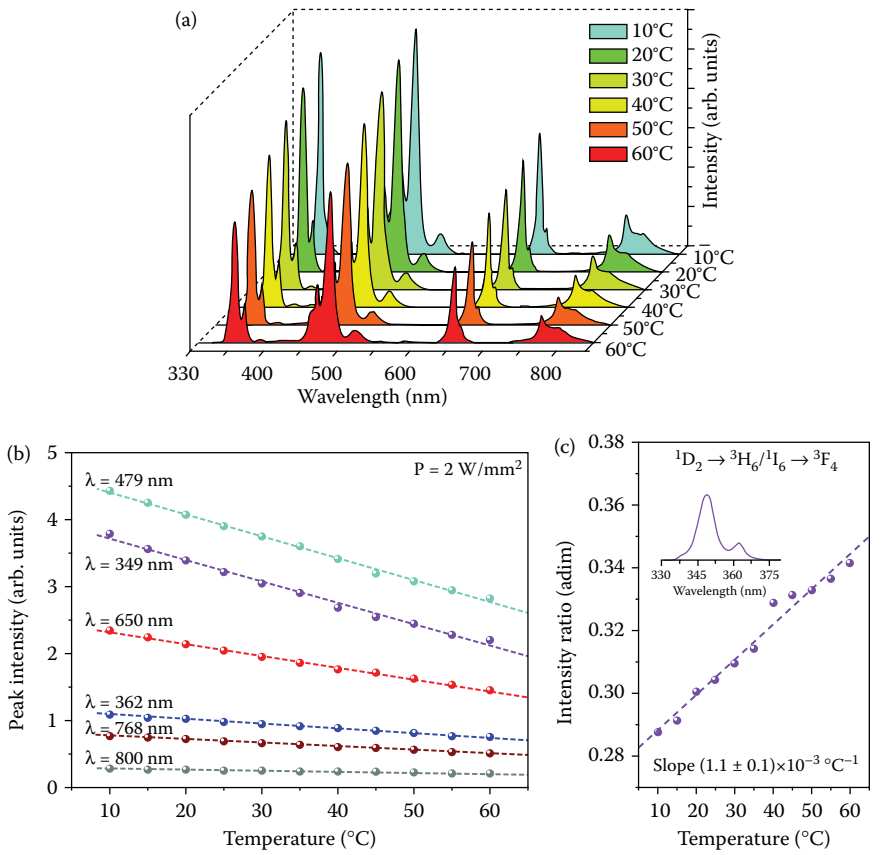

FIGURE 11.7
(a) Overall temperature dependence of the upconversion emission spectrum and (b) peak intensities of the main emission bands as a function of the temperature of SrF_2:Tm^{3+}/Yb^{3+} UCNPs in a colloidal dispersion in D_2O. The dashed lines in the lower graph have been added to guide the eye. (c) UV-based *LIR* ($^1D_2 \rightarrow {}^3H_6/{}^1I_6 \rightarrow {}^3F_4$). The inset shows the corresponding spectral range. The dashed lines are the linear fit of the experimental data. The corresponding slopes are also given in the graph. (Quintanilla, M. et al. 2015. Intense ultraviolet upconversion in water dispersible SrF_2: Tm^{3+}, Yb^{3+} nanoparticles: The effect of the environment on light emissions. *J. Mater. Chem. C* 3:3108–13. Reproduced by permission of The Royal Society of Chemistry.)

It becomes obvious that the overall emission intensity decreases with increasing temperature (Figure 11.7a). However, the extent to which this decrease happens is found to vary from peak to peak, especially in case of the NIR emission from the $^3H_4$ level and the UV emission attributed to the $^1D_2$ level (362 nm) (Figure 11.7b). These differences are related to different excitation paths in which the states are populated; increase of multiphonon relaxation processes on the one hand and favored phonon-assisted energy transfer processes on the other hand, particularly important in the population of the $^1D_2$ state by non-resonant Yb^{3+}–Tm^{3+} energy transfer and Tm^{3+}–Tm^{3+} cross-relaxation processes. Thus, in principle, thermal sensing would be possible by using graphs given in Figure 11.7b as temperature calibration curves. However, in order to overcome drawbacks related to intensity-based nanothermometers (see Introduction), the more reliable *LIR* technique has successfully been applied using the ratio between the intensities originating from the $^1D_2 \rightarrow {}^3H_6$ and $^1I_6 \rightarrow {}^3F_4$ transitions (Figure 11.7c).

11.3.3 Ho^{3+}-Based Nanothermometers

Optical temperature sensing based on upconversion emission has further been reported for Ho^{3+}-based phosphors. Most of the published work body is dedicated to Ho^{3+}-doped glasses or ceramic host materials (Du et al. 2015a, b; Singh 2007; Verma and Rai 2012; Xu et al. 2012a, 2013a), while studies on upconverting micro- or nanoparticles (e.g., Yb^{3+}/Ho^{3+} co-doped $NaLuF_4$ microcrystals [Zhou et al. 2014c] or Yb^{3+}/Ho^{3+}co-doped Y_2O_3 UCNPs [Lojpur et al. 2013]) are much less frequent. Generally, these nanothermometers are either based on the temperature dependent population of thermally coupled energy levels (green $^5F_4/^5S_2 \rightarrow {}^5I_8$ emissions, blue $^5F_{2,3}/^3K_8 \rightarrow {}^5I_8$ and $^5F_1/^5G_6 \rightarrow {}^5I_8$ emissions, Figure X.2c) or on the temperature dependence of the ratio between the overall green ($^5F_4/^5S_2 \rightarrow {}^5I_8$) and NIR ($^5F_4/^5S_2 \rightarrow {}^5I_7$) emission.

As an example of very recent work on Ho^{3+}-doped UCNPs for nanothermometry, a study by Savchuk et al. (2015) should be highlighted here. The authors developed a Ho^{3+}/Yb^{3+} co-doped KLuW nanothermometer that shows outstanding versatility since one single probe material offers different thermal sensing techniques, thus providing a way to corroborate temperature measurements. These include the *LIR* technique of two thermally coupled Stark sub-levels, the intensity ratio between the red and green luminescence bands, the observation of the change of the color of the emitted light arising from the UCNPs, and lifetime measurements (Figure 11.8). Figure 11.8a1 shows the temperature dependence of the red emission band that consists of two peaks assigned to the radiative transition from different Stark sub-levels of the $^5F_5$ energy level to the $^5I_8$ ground state of Ho^{3+}. Due to the small energy gap between the two thermally coupled Stark sub-levels, the upper sub-level can be thermally populated from the lower sub-level when the temperature increases. Consequently, the *LIR* (here denoted as

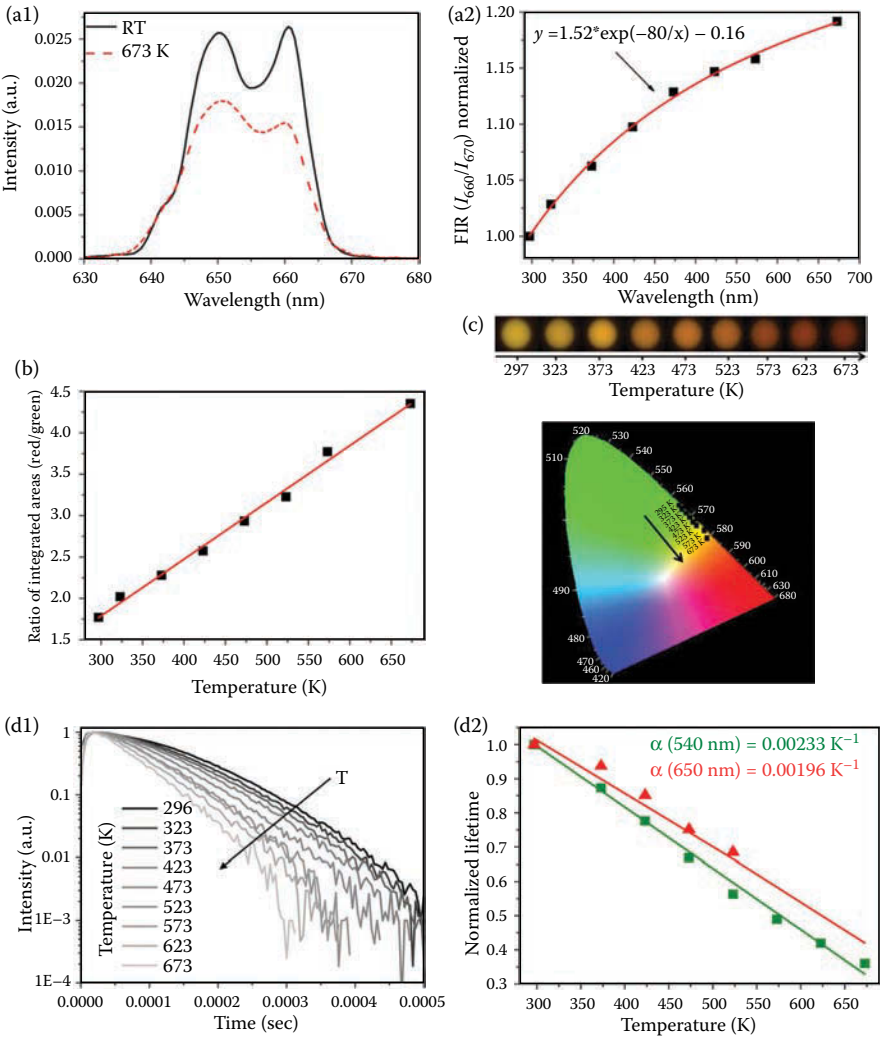

FIGURE 11.8

Ho^{3+}/Yb^{3+} co-doped KLuW-based nanothermometry. (a) Red Stark sub-level emission ($^5F_5 \rightarrow {}^5I_8$; a1: emission spectra at room temperature and 673 K; a2: *T*-dependent *LIR* of the I_{650}/I_{660}). (b) Ratio of integrated areas between the red ($^5F_5 \rightarrow {}^5I_8$) and green ($^5S_2/^5F_4 \rightarrow {}^5I_8$) emission bands as the function of *T*. (c) Color perception of the emission arising from the sample. (d) *T* dependence of the lifetime (d1: fluorescence decay curves corresponding to the 540 nm emission line associated with the $^5S_2/^5F_4$ radiative transition; d2: normalized lifetime values as a function of *T*). (Reprinted with permission from Savchuk, O. A. et al. 2015. Ho,Yb:KLu$(WO_4)_2$ nanoparticles: A versatile material for multiple thermal sensing purposes by luminescent thermometry. *J. Phys. Chem. C* 119, 18546–58. Copyright 2015 American Chemical Society.)

FIR, fluorescence intensity ratio) can be determined as a function of temperature, revealing that the experimental data can be well fitted by Boltzmann's distribution (Figure 11.8a2). In contrast to this intensity ratio of the emissions originating from the Stark sub-levels, the ratio of the integrated areas between the overall red ($^5F_5 \rightarrow {}^5I_8$) and green ($^5S_2/^5F_4 \rightarrow {}^5I_8$) emission bands (Figure 11.8b) follows a linear temperature dependence. A characteristic of such linear temperature dependence is the fact that it ensures a constant thermal sensitivity in the whole working temperature range of the thermal probe, which simplifies calibration of the nanothermometer. It must further be mentioned, that the two excited states considered here are located too far from each other for thermal coupling. Therefore, the populations of the green and red emitting excited states do not follow a Boltzmann's distribution, and the *LIR* technique cannot be applied. However, the population of the $^5F_5$ electronic level of Ho^{3+} mainly arises from the non-radiative relaxation from the $^5S_2$ and $^5F_4$ levels; a process that is temperature dependent. Thus, the $^5F_5$ and the $^5S_2$ as well as $^5F_4$ levels are considered as electronically coupled, which is expressed by the plot of the thermal evolution of I_{red}/I_{green} depicted in Figure 11.8b. It has further been observed that the color perception of the emission arising from the Ho^{3+}/Yb^{3+}:KLuW UCNPs changes from yellow to dark orange (Figure 11.8c), which was suggested as a new possibility for visual temperature determination, although the authors critically mention that the thermal resolution would be very wide, of the order of 50 K, if it is intended to be visualized by the naked eye. Finally, the prepared UCNPs were used for lifetime-based nanothermometry by measuring the decay curves corresponding to the 540 nm emission line associated with the $^5S_2/^5F_4$ radiative transition (Figure 11.8d1). Rising times in these curves indicate the occurrence of energy transfer processes, while the observation of a non-single exponential component indicates the existence of non-radiative processes that are responsible for the reduction of the lifetime with increasing temperature. Remarkably, the normalized lifetimes for the emission lines centered at 540 and 650 nm depicted in Figure 11.8d2 show a linear temperature dependence, thus a temperature independent thermal sensitivity. In fact, while the *LIR* technique revealed the highest sensitivity of the presented UCNPs at room temperature, the intensity ratio technique comparing the green and red emission intensities as well as the lifetime-based approach show a constant thermal sensitivity over the evaluated temperature range, which would allow for simplified calibration and for more precise measurements at higher temperatures.

11.3.4 Nd^{3+}-Based Nanothermometers

As a last representative of the group of Ln^{3+} ions applied in nanothermometry, Nd^{3+}-based phosphors should be briefly discussed. In case of Nd^{3+}/Yb^{3+} co-doped phosphors under 980 nm illumination, as depicted in Figure 11.2d, the population of the Nd^{3+} excited levels does not follow an

upconversion mechanism but a phonon-assisted energy transfer process from the $^5F_{5/2}$ excited level of Yb^{3+} to the $^4F_{3/2}$ excited level of Nd^{3+} caused by the energy mismatch between the electronic levels involved. Subsequently, radiative relaxation can take place from the NIR emitting levels of Nd^{3+}. In fact, it is this emission of NIR light that trigged an increasing interest in Nd^{3+}-doped phosphors when seeking optical probes for biomedical application. The reasoning behind this is, again, the fact that NIR light is less scattered and absorbed by water and biological matter than visible or UV light resulting in advanced transparency of biological tissues toward NIR. This ultimately opens new avenues for the use of optical probes in the biomedical field. Moreover, as seen in Figure 11.2d, the energy gaps between the $^4F_{3/2}$, $^4F_{5/2}$, and $^4F_{7/2}$ levels are relatively small, so that the $^4F_{5/2}$ and $^4F_{7/2}$ states can be thermally populated from their lower energy levels. This makes them suitable for thermal sensing. For instance, the group of W. Cao studied the temperature dependence of the NIR emissions originated from the $^4F_{7/2}/^4S_{3/2} \rightarrow {}^4I_{9/2}$ (~750 nm), $^4F_{5/2}/^2H_{9/2} \rightarrow {}^4I_{9/2}$ (~803 nm), and $^4F_{3/2} \rightarrow {}^4I_{9/2}$ (~863 nm) transitions of Nd^{3+} ions in Nd^{3+}/Yb^{3+} co-doped oxyfluoride glass ceramic (Xu et al. 2013b) and in $CaWO_4$ powder (Xu et al. 2014) under 980 nm laser excitation.

In another study, Wawrzynczyk et al. (2012) used a 830 nm laser for the direct excitation of Nd^{3+} ions in heavily Nd^{3+}-doped $NaYF_4$ nanoparticles. Thermal sensing was reported by monitoring the absolute NIR luminescence intensity or by measuring the intensity ratio of the two Stark sub-levels of the $^4F_{3/2}$ multiplet in the Nd^{3+} ions. Based on their findings, the authors formulated two main advantages of the proposed nanothermometers. First, the possibility of using NIR light for the excitation and emission wavelength allows for a performance fully in the optical transmission tissue penetration window. This window, also known as the *biological window*, encompasses three distinct wavelength NIR regions, namely 700–950 nm (NIR-I), 1000–1350 nm (NIR-II), and 1550–1870 nm (NIR-III), in which the scattering and absorption of light by water, blood, and various biological tissues is significantly reduced when compared to UV or visible light (Anderson and Parrish 1981; Prodi et al. 2015; Sordillo et al. 2014; Smith et al. 2009). This allows for deeper penetration depth and enhanced propagation of NIR light through biological samples making NIR emitting probes highly attractive for optical bioimaging (Diao et al. 2015; Hemmer et al. 2013a, 2016; Yao et al. 2014). Second, the proposed nanothermometers provide the possibility for excitation intensity dependent heating (high excitation regime) on the one hand and thermal sensing (low excitation) on the other. Following this idea, recent research efforts focus on the development of Nd^{3+}-doped nanothermometers and nanoheaters for biomedical applications that operate in the NIR region taking advantage from reduced scattering and absorption by biological tissues when compared to UV or visible light (Carrasco et al. 2015; Ceron et al. 2015; Marciniak et al. 2015; Rocha et al. 2014).

11.3.5 Nanothermometers Based on the Combination of Different Ln^{3+} Ions

The use of co-dopants (e.g., Mn) for enhanced thermal sensing performance was mentioned in Section 11.3.1. In this section, the focus will be set on the combination of various Ln^{3+} ions and the advantage that can be taken from energy transfer processes between different Ln^{3+} ions for the development of novel nanothermometers.

Co-doping with two different Ln^{3+} ions with close laying energy levels in one host material and the use of the *LIR* between the two emissions originating from these levels for nanothermometry was reported by Pandey and Rai (2013). In $Ho^{3+}/Tm^{3+}/Yb^{3+}$ co-doped Y_2O_3, the $^5F_3$ excited level of Ho^{3+} and the $^1G_4$ excited level of Tm^{3+} are populated through energy transfer from the excited $^5F_{5/2}$ Yb^{3+} level to the Ho^{3+} and Tm^{3+} ions. Since these two excited states of Ho^{3+} and Tm^{3+} are very close to each other, exhibiting a narrow energy gap of 473 cm^{-1}, a thermal variation changes the population of the levels and consequently the emission intensities. It was shown that the population of both blue emitting levels follows Boltzmann's distribution, and the *LIR* technique was applied revealing a maximum sensitivity of $6.96 \cdot 10^{-3}$ K^{-1} at 303 K.

The combination of appropriate Ln^{3+} ions can further enable emissions that are not possible otherwise. For instance, Gd^{3+} ions in the ground state cannot absorb 980 nm photons directly because of the large energy gap between the ground state $^8S_{7/2}$ and the first excited, UV emitting states ^6P_J. In order to foster UV emission from the excited Gd^{3+} states, Zheng et al. (2013) prepared $NaLuF_4$ microcrystals that were co-doped with Yb^{3+} and Tm^{3+} in addition to Gd^{3+}. The use of Tm^{3+} ions as sensitizers resulted in the population of the excited states ^6I_J of Gd^{3+} through an energy transfer process from Tm^{3+} ($^3P_2 \rightarrow {}^3H_6$) to Gd^{3+} ($^8S_{7/2} \rightarrow {}^6I_J$) (Figure 11.9a).

Additionally, the ^6P_J and ^6D_J Gd^{3+} levels can be populated by non-radiative relaxation process of ^6I_J to ^6P_J and by energy transfer of Yb^{3+}/Gd^{3+} and Tm^{3+}/Gd^{3+}. With regards to nanothermometry, it is important that the narrow spacing between the Gd^{3+} excited levels favors the thermal population of the ^6P_J ($^6P_{5/2}$, $^6P_{7/2}$) and ^6I_J ($^6I_{13/2}$, $^6I_{15/2}$, $^6I_{11/2}$, $^6I_{9/2}$, $^6I_{7/2}$) sub-levels, allowing for the application of the *LIR* technique for UV-based thermal sensing. Maximum sensitivity values of about 0.0004 K^{-1} (at 333 K) where obtained when exploiting the *LIR* between $^6P_{5/2}$ and $^6P_{7/2}$ levels and 0.0029 K^{-1} (at 298 K) for the *LIR* between $^6I_{9/2}$ and $^6I_{7/2}$ levels. In addition to the suitability for thermal sensing, the potential for optical (based on Tm^{3+}) and MR imaging (based on Gd^{3+}) is identified, which makes the reported $Gd^{3+}/Tm^{3+}/Yb^{3+}$ co-doped $NaLuF_4$ phosphor a promising platform for multimodal biomedical applications.

Following a similar idea exploiting energy transfer between different Ln^{3+} ions, Zheng et al. (2014) designed a ratiometric optical nanothermometer that combines different Ln^{3+} ions in one core–shell UCNP. The combination of a Tm^{3+}/Yb^{3+} co-doped $NaGdF_4$ core with a Tb^{3+}/Eu^{3+} co-doped $NaGdF_4$

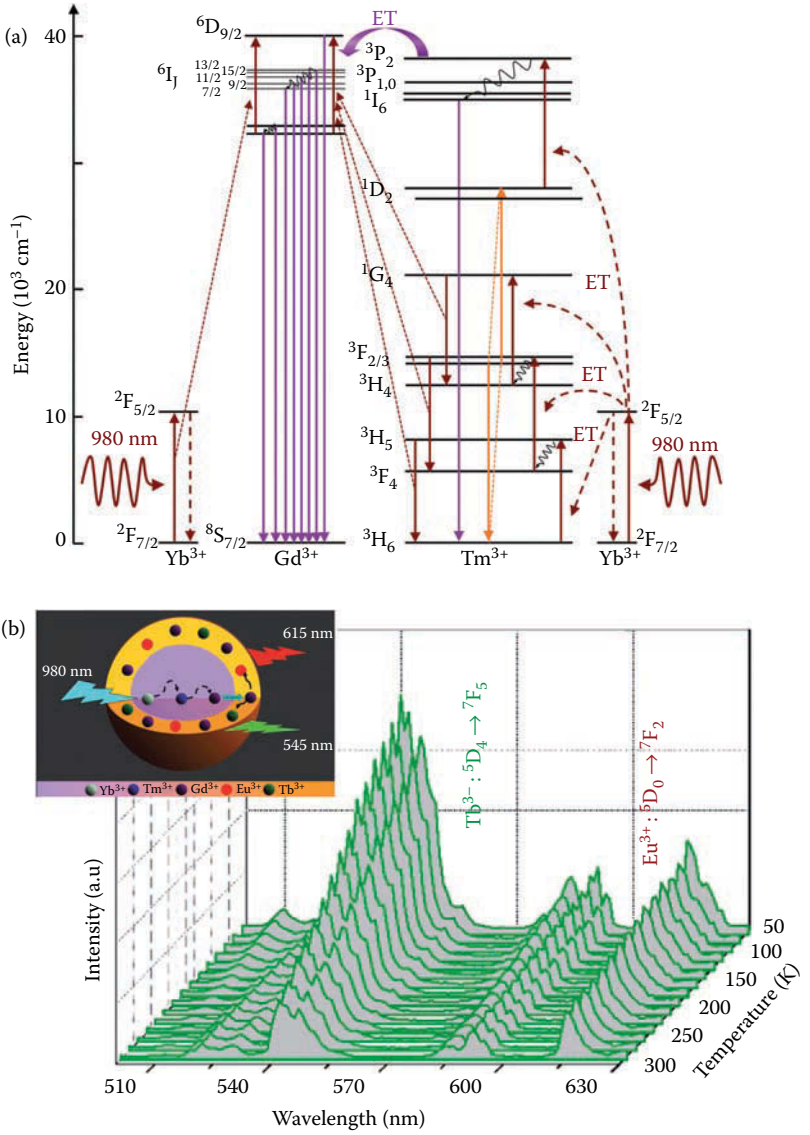

FIGURE 11.9
Multiple Ln^{3+} doping for UCNP-based nanothermometry. (a) Energy level diagrams of Yb^{3+}, Tm^{3+}, and Gd^{3+} ions, and possible upconversion processes. (Zheng, K. Z., Z. Y. Liu, C. J. Lv, and W. P. Qin. 2013. Temperature sensor based on the UV upconversion luminescence of Gd^{3+} in Yb^{3+}-Tm^{3+}-Gd^{3+} codoped $NaLuF_4$ microcrystals. *J. Mater. Chem. C* 1:5502–07. Reproduced by permission of The Royal Society of Chemistry.) (b) *T*-dependent green and red upconversion emission spectra of $NaGdF_4$:Tm^{3+}/Yb^{3+}@$NaGdF_4$:Tb^{3+}/Eu^{3+} core–shell nanoparticles under 980 nm excitation. (Zheng, S. H. et al. 2014. Lanthanide-doped $NaGdF_4$ core–shell nanoparticles for non-contact self-referencing temperature sensors. *Nanoscale* 6:5675–79. Reproduced by permission of The Royal Society of Chemistry.)

shell allows for the highly temperature sensitive generation of green and red emission upon NIR excitation (Figure 11.9b). The Tm^{3+} ions are excited to the $^1I_6$ level via a five-photon upconversion process from the excited Yb^{3+} ions in the $^5F_{5/2}$ level, followed by energy transfer to the $^6P_{7/2}$ Gd^{3+} level, from where energy is transferred in order to populate the ^5D_J levels of the Tb^{3+} and Eu^{3+} ions. The emission intensity originating from the $^5D_4 \rightarrow {}^7F_5$ transition (Tb^{3+} at 545 nm) shows a linear temperature dependence, whereas the $^5D_0 \rightarrow {}^7F_2$ transition (Eu^{3+} at 615 nm) is much less affected by temperature changes. Consequently, the *LIR* between these two emissions could be used for self-referencing nanothermometry.

Aiming for *in vivo* nanothermometry, the different optical properties of biological tissues, and scattering and absorption of the used light are a challenge. Addressing this, Klier and Kumke (2015b) exploited the increased penetration depth of ~800 nm light when compared to 980 nm light and investigated the influence of the excitation wavelength on the thermal behavior of Er^{3+}/Yb^{3+}:$NaYF_4$ UCNPs co-doped with Gd^{3+} and Nd^{3+}. In this system, Nd^{3+} ions are excited from their $^4I_{9/2}$ to the $^4F_{5/2}$ energy level, followed by a non-radiative relaxation step to the $^4F_{3/2}$ level of Nd^{3+}. Subsequent energy transfer takes place from this excited Nd^{3+} level to the $^2F_{5/2}$ level of the Yb^{3+} ions, followed by regular upconversion processes resulting in the characteristic green and red Er^{3+} emissions. Investigation of the heating and sensing capability of the Nd^{3+} co-doped probes revealed that the excitation with 795 nm induced no optical heating, while 980 nm illumination (170 mW excitation power for both wavelengths) resulted in a temperature increase of ΔT ~0.6 K, which may trigger cell death. The thermal sensitivity was found to be almost unaffected by the choice of excitation wavelength. Thus, Nd^{3+}-sensitized phosphors can offer an attractive alternative when optical heating must be avoided.

11.4 Nanothermometers Based on Multicomponent Nanoassemblies: Toward Sensitivity Enhancement and Multimodal Biomedical Applications

During the last few years, worldwide effort has been undertaken in the search for temperature sensitive phosphors that are suitable for thermal sensing down to the sub-micron scale. In this context, Ln^{3+}-based upconverting materials have been recognized as potential nanothermometers that are expected to open new pathways in the field of thermal sensing, with particular emphasis in the biomedical field, for example, sub-cellular thermal mapping or temperature monitoring in the frame of thermal therapeutic approaches. Seeking enhanced sensitivity in the biologically relevant temperature range and/or multimodality is a challenge that has been most recently addressed by researchers in the field. Here, the assembly of UCNP-based

thermal sensors with a second moiety, such as an organic dye, a thermoresponsive polymer or metal nanostructures, provides attractive possibilities for the design of application-oriented multifunctional nanoplatforms.

11.4.1 UCNP–Organic Hybrids for Improved Sensitivity

Chen et al. (2013) used the concept of LRET in order to achieve a multicolor hybrid nanothermometer based on Er^{3+}/Yb^{3+} co-doped $NaYF_4$ UCNPs and the organic dye rhodamine 6G (R6G). Due to the spectral overlap between the green Er^{3+} emission and the absorption band of R6G, energy can be transferred resonantly from the Er^{3+} ions to the R6G dye. In the case where the energy donors (Er^{3+} ions) and the energy acceptors (R6G dye) are in close enough proximity, the energy transfer takes place non-radiatively. In addition, radiative energy transfer takes place where some of the emitted photons from the $^2H_{11/2} \rightarrow {}^4I_{15/2}$ and $^4S_{3/2} \rightarrow {}^4I_{15/2}$ transitions are reabsorbed by the R6G, and excite the electrons in R6G from the highest occupied molecular orbital to the lowest unoccupied molecular orbital. Subsequent radiative recombination gives rise to the R6G emission. Implementation of these UCNP–dye hybrids in self-assembled hemispherical microstructures led to an intensity-based nanothermometer demonstrating better thermal sensitivity than the pure UCNPs, which was assigned to the energy transfer between UCNPs and R6G.

Alternatively, J. C. Huang et al. (2015) opted for a hydrogel obtained by modification of Er^{3+}/Yb^{3+} co-doped $NaYF_4$ UCNPs with the thermoresponsive polymer poly(N-isopropylacrylamide) (pNIPAM) cross-linked with poly(acrylamide) (pAAm) that could be applied for intensity-based nanothermometry. At temperatures higher than the transition T of pNIPAM, the polymer chains undergo a reversible coil-globule phase transition resulting in increased opacity of the hydrogel. The observed thermal sensitivity was linked to the reduction of the detectable upconversion emission caused by this higher opacity of the hydrogel when T was higher than the transition T of pNIPAM.

The combination of thermoresponsive polymer pNIPAM and a LRET pair for thermal sensing was suggested by Hemmer et al. (2015). In their strategy, the surface of Er^{3+}/Yb^{3+} co-doped $NaGdF_4$ UCNPs (acting as energy donors) was modified with pNIPAM and subsequently conjugated with the organic dye FluoProbe532A (acting as an energy acceptor). Here, the use of pNIPAM as a temperature responsive linker between the UCNPs and the dye molecules adds additional thermal sensitivity to the system. Most importantly, it was shown that with the increase of the temperature, the collapse of the pNIPAM polymer chains led to closer proximity between the UCNP/dye pair (Figure 11.10a) that eventually results in the decrease of the green emission intensity due to more effective energy transfer processes (Figure 11.10b). In other words, the efficiency of the energy transfer between the donor UCNP and the acceptor dye is controlled by the spatial distance between both moieties, which is itself controlled by the temperature dependent collapsing

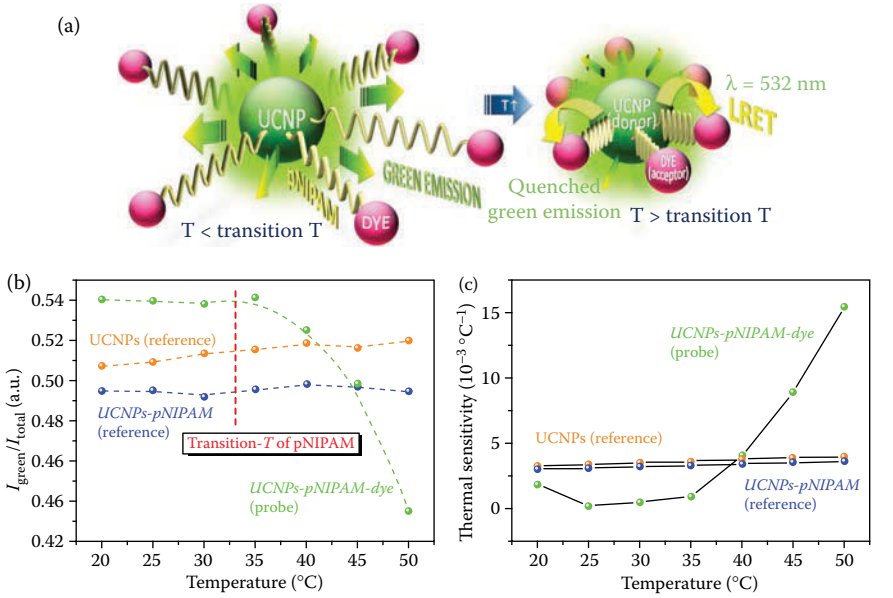

FIGURE 11.10
(a) Scheme of the LRET system based on Er^{3+}/Yb^{3+} co-doped $NaGdF_4$ UCNPs, thermoresponsive polymer pNIPAM and organic dye FluoProbe532A. (b) *T*-dependence of the relative green emission from Er^{3+}/Yb^{3+} co-doped $NaGdF_4$ UCNPs (energy donors) modified with pNIPAM and conjugated with an organic dye (energy acceptor) under 980 nm laser excitation. The *LIR* was defined as the ratio between the green emission intensity (wavelength region: 496–580 nm) versus the total upconversion emission (wavelength region: 300–840 nm). (c) Estimated thermal sensitivity of the UCNPs–pNIPAM–dye probe (reference probes: pNIPAM modified UCNPs without dye and unmodified UCNPs). (Reprinted with permission from Hemmer, E. et al. 2015. Temperature-induced energy transfer in dye-conjugated upconverting nanoparticles: A new candidate for nanothermometry. *Chem. Mater.* 27, 235–44. Copyright 2015 American Chemical Society.)

or stretching of the pNIPAM chains. Estimation of the thermal sensitivity revealed a significant increase when reaching temperatures above the polymer's transition temperature of 35°C (which is in close proximity to a *T* range of biological interest) compared to UCNPs without the dye acceptor unit (Figure 11.10c). The use of a thermoresponsive polymer with a tailored transition temperature below 35°C is expected to induce a shift of the observed improved thermal sensitivity toward the physiologically highly interesting range of ~37°C.

11.4.2 Multifunctional Nanoplatforms for Optical Heating and Thermal Sensing

The effect of optical heating in Ln^{3+}-doped UCNPs has already been mentioned in the previous sections of this chapter. We could see that, dependent

on the conditions under which the nanothermometers are applied, this heating effect must be considered as good (e.g., when aiming for controlled heating at the sub-micron scale) or evil (e.g., when affecting the accuracy of the thermometer or inducing death of healthy cells). During the last few years, light-induced thermal heating has gained particular interest in the biomedical field since photothermal methods open new therapeutic approaches (Cheng et al. 2014; Jaque et al. 2014a; Melamed et al. 2015; Shanmugam et al. 2014). Furthermore, aiming for controlled heating at a (sub-)cellular level, plasmon-induced nanoheaters were recognized as attractive candidates. For the application of such nanoheaters in nanomedicine, high spatial (10^{-6} m) and temperature (10^{-1} degree) resolution is most crucial and still challenging (Debasu et al. 2013). This has a twofold advantage where (i) careful monitoring of the thermal profile guarantees strong enough heating in regions where desired, for instance in tumorous tissues, while (ii) simultaneously providing the spatial limitation to exactly the region requiring treatment in order to avoid damage of healthy tissues and cells in the vicinity. In this context, the combination of Ln^{3+}-doped nanoparticles as nanothermometers with gold nanostructures as nanoheaters has been suggested. For example, Rocha et al. (2013) provided the first demonstration of a single-beam sub-tissue-controlled heating process (sub-tissue hyperthermia process) based on the combination of Nd^{3+}:LaF_3 nanoparticles and gold nanorods (GNRs) that act as nanothermometers, and nanoheaters respectively. Shortly after, the decoration of Er^{3+}/Yb^{3+} co-doped Gd_2O_3 nanorods with gold nanoparticles (AuNPs) as an all-in-one nanoplatform was suggested by Debasu et al. (2013). This approach combined for the first time nanoheaters and nanothermometers in one composite nanoassembly (Figure 11.11a). When the heaters and the sensors are separate in space, for instance when the individual components are dispersed together in solution, an average temperature of the sample volume under irradiation is measured since the recorded emission spectra include the contribution of those emitting particles that are away from the heaters, and thus undergo less heating than those particles in close proximity to the heaters. However, when the heaters and the sensors constitute a single integrating nanoplatform, such as in the presented nanoassembly, the absolute local temperature can be measured as the heaters and sensors are not spatially separated from each other. In these nanoassemblies, the surface temperature detected by the upconverting nanorods was adjusted by controlling the amount of AuNPs on their surface, where a higher concentration of AuNPs induced a more pronounced heating effect. Concerning the heating mechanism, evidence was found for direct (980 nm, used for excitation of the Er^{3+}) and multiphoton absorption, probably involving interband transitions of Au. Aside, heating was assigned to the Au absorption of the green Er^{3+} emission (510 to 565 nm), which is in resonance with the localized surface plasmon resonance of Au. The local temperature was then monitored with the help of the *LIR* technique using the Boltzmann's distribution of the intensity ratio between the $^2H_{11/2} \rightarrow {}^4I_{15/2}$ and $^4S_{3/2} \rightarrow {}^4I_{15/2}$ Er^{3+} transitions.

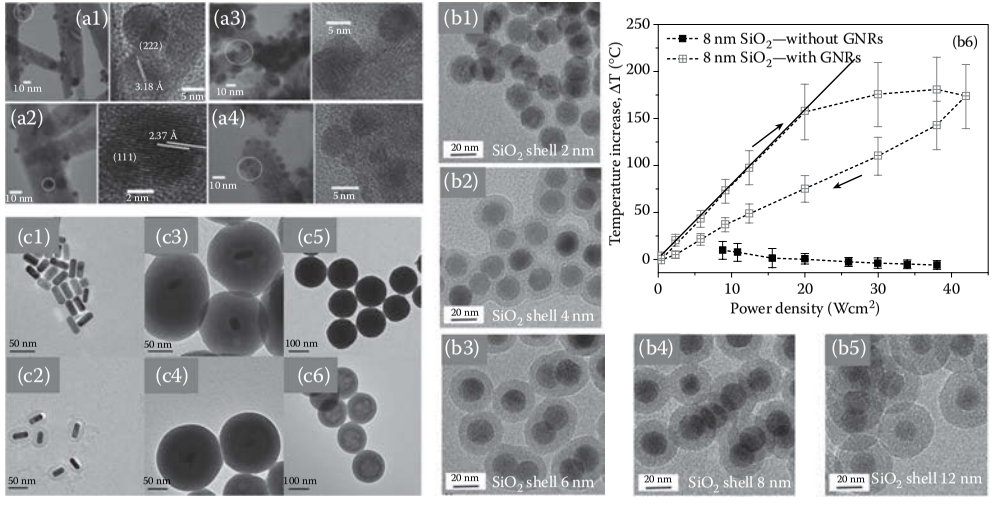

FIGURE 11.11

Selected nanoplatforms for optical heating and thermal sensing based on Ln^{3+} upconverting and gold nanostructures. (a) Transmission electron microscopy (TEM) images of an all-in-one Er^{3+}/Yb^{3+}:Gd_2O_3-AuNPs nanocomposites with different nominal gold amount: (a1) 1.25, (a2) 2.5, (a3) 12.5, and (a4) 25 µmol Au. The images on the right-hand side magnify the regions depicted by the white circles on the left. (Debasu, M. L. et al.: All-in-one optical heater-thermometer nanoplatform operative from 300 to 2000 K based on Er^{3+} emission and blackbody radiation. *Adv. Mater.* 2013. 25. 4868–74. Copyright Wiley-VCH Verlag GmbH & Co. KGaA. Reproduced with permission.) (b) Plasmonic heating and thermal sensing based on Er^{3+}/Yb^{3+} co-doped $NaGdF_4$and GNRs: (b1–b5) TEM image of Er^{3+}/Yb^{3+}:$NaGdF_4$ with different SiO_2 shell thicknesses of 2–12 nm. (b6) Calculated temperatures at different excitation powers for 8 nm SiO_2-coated samples with and without GNRs. The dashed line is added to guide the eye. The straight line is the theoretical fit of the data before deformation of the GNRs (Rohani, S. et al.: Enhanced luminescence, collective heating, and nanothermometry in an ensemble system composed of lanthanide-doped upconverting nanoparticles and gold nanorods. *Adv. Opt. Mater.* 2015. 3. 1606–13. Copyright Wiley-VCH Verlag GmbH & Co. KGaA. Reproduced with permission.) (c) Nanoheating and -sensing GNR-Er^{3+}/Yb^{3+}:$NaYF_4$ nanocomposite: TEM images of (c1) GNRs, (c2) SiO_2-coated GNRs, (c3) GNRs with a SiO_2 and Er^{3+}/Yb^{3+}:$Y(OH)CO_3$ shell, (c4) GNRs with a SiO_2 and Er^{3+}/Yb^{3+}:$NaYF_4$ shell, (c5) Er^{3+}/Yb^{3+}:$Y(OH)CO_3$, and (c6) Er^{3+}/Yb^{3+}:$NaYF_4$ hollow nanoshells. (Huang, Y., Federico R., and Fiorenzo V. 2015. A single multifunctional nanoplatform based on upconversion luminescence and gold nanorods. *Nanoscale* 7:5178–85. Reproduced by permission of The Royal Society of Chemistry.)

Obtained thermal resolutions reached from 0.3 to 2.0 K in the range 300–1050 K including the biologically relevant temperature range.

Further, in the search for methods to improve the photoluminescence efficiency of UCNPs, plasmon enhancement by use of Au nanostructures has been reported. In fact, GNRs create a localized electromagnetic field that can enhance the emission intensity from UCNPs. Here, the distance between the upconverter and the Au nanostructure is an essential parameter. Very recently, Rohani et al. (2015) developed a nanothermometry–nanoheating platform based on SiO_2-coated Er^{3+}/Yb^{3+} co-doped $NaGdF_4$ UCNPs and GNRs. The longitudinal surface plasmon resonance of the GNRs was tuned to 980 nm, in resonance with the Yb^{3+} absorption wavelength, so the GNRs and the UCNPs can be simultaneously excited. Moreover, the variation of the SiO_2 shell thicknesses allowed tuning of the minimum distance between the UCNPs and the GNR (Figure 11.11b1–5). Investigating the effect of the SiO_2 shell thickness on the plasmon-induced upconversion enhancement, an optimized shell thickness of 8 nm was found. Besides, excitation with 980 nm triggers heat generation from the GNRs that is controlled by the chosen laser power and monitored by the *LIR* technique using the $^2H_{11/2} \rightarrow {}^4I_{15/2}$ and $^4S_{3/2} \rightarrow {}^4I_{15/2}$ emission bands of Er^{3+} ions. While no heat increase was observed in SiO_2-coated UCNPs without GNRs, regardless of the applied excitation power, a temperature increase by 4°C to 170°C was observed in the sample consisting of SiO_2-coated UCNPs and GNRs upon increase of the laser power density from 2 W cm^{-2} to 42 W cm^{-2} (Figure 11.11b6). Up to a power density of 20 W cm^{-2}, linear behavior of the temperature increase was observed, while reduced heat generation was found for higher power densities. This observation was assigned to the deformation of GNRs at elevated temperatures, which is an important finding in terms of practical applications of nanoheaters for the higher temperature range. Overall, upconversion enhancement and effective heating performance of GNRs as well as *in situ* thermal sensing with UCNPs was demonstrated, providing a new perspective to nanoscale sensors that can be potentially used in photothermal therapy.

A different strategy to combine plasmonic heating and optical nanothermometry presented by Y. Huang et al. (2015) consists of a multifunctional nanoplatform composed of a GNR core and an outer hollow shell of upconverting Er^{3+}/Yb^{3+} co-doped $NaYF_4$ (Figure 11.11c). In this approach, the aspect ratio of the GNRs corresponds to a longitudinal surface plasmon resonance at 654 nm, which is in good overlap with the 980 nm induced red $^4F_{9/2} \rightarrow {}^4I_{15/2}$ emission from Er^{3+} ions doped into the outer shell. Thus, upon optical illumination with 980 nm, the upconverting shell emits light of ~660 nm wavelength that subsequently is absorbed by the GNRs due to surface plasmon resonance and eventually triggers the rapid plasmonic heat formation in the GNRs. The energy transfer from the excited Er^{3+} to the GNRs was further obvious from a quenching of the red emission band in the upconversion spectrum by 61.8% when compared to nanoshell Er^{3+}/Yb^{3+}:$NaYF_4$ structures without GNRs. Simultaneously, the thermal change was monitored by use of

the green emission bands ($^2H_{11/2} \rightarrow {}^4I_{15/2}$ and $^4S_{3/2} \rightarrow {}^4I_{15/2}$) from Er^{3+} ions following the *LIR* technique revealing a temperature increase by 9°C upon excitation of the GNRs-Er^{3+}/Yb^{3+}:$NaYF_4$ core–shell system with 980 nm. Finally, the authors went one step further evaluating the potential of their nanostructure for drug delivery. Therefore, the anticancer drug doxorubicin was loaded into the GNRs-Er^{3+}/Yb^{3+}:$NaYF_4$ nanocomposites and the drug release profile evaluated. It was found that the photothermal effect (thus increased temperature) as described before, could trigger fast drug release, especially at low pH values, conditions that are found in tumor extracellular environments, which makes the suggested strategy promising for applications in cancer therapy.

11.5 Conclusions

In conclusion, since the first mention of Ln^{3+}-based nanothermometry in 2002 by Wang et al. (2002) the field of optical nanothermometry has clearly seen significant impact through the development of novel dopant/host combinations for improved sensitivity in application-oriented temperature ranges, assembly of multifunctional nanoplatforms allowing for simultaneous heating, thermal sensing and imaging, and first proofs of concept by *in vivo* and *ex vivo* applications.

Challenges that will have to be addressed by future studies include simultaneous control over the thermal and spatial resolution, especially when aiming for nanothermometry at a sub-cellular level in the biomedical field. Previous achievements raise high expectations that lanthanide-doped UCNPs provide the necessary performance to fulfill this task. Yet, for biomedical applications, an additional vital aspect is the nanothermometers' biocompatibility. The various strategies applying surface modification, for instance with poly(ethylene glycol), amine groups, or SiO_2, (Hemmer et al. 2013a, b, 2014; Ju et al. 2012; Shan et al. 2008; Zhang et al. 2015) have been followed to address potential toxicity issues of UCNPs. However, surface modification of UCNPs raises new questions such as its influence on thermal performance of the sensors or its stability when optical heating applies. As shown, uncontrolled optical heating leading to thermally induced damage of healthy biological tissue can be overcome by the choice of the appropriate excitation wavelength. Moreover, NIR light in the biological window has been recognized as advantageous over visible light for bioimaging applications (Diao et al. 2015; Hemmer et al. 2013a, 2016; Yao et al. 2014) since it poses advanced penetration capabilities through biological tissues due to reduced scattering and absorption by water and biological tissues. Consequently, NIR-based nanothermometers will be of particular interest for *in vivo* applications where exciting and emitted light have to pass through thicker layers of various biological tissues.

This led to the first application of the concept of nanothermometry in the NIR region. Based on the very promising results from these early studies, a future shift from upconversion-based to NIR light-based nanothermometry may be likely. Finally, the combination of obtained sensing and heating nanostructures with other modalities such as the potential for magnetic imaging or drug delivery will result in truly multimodal platforms.

Overall, the striking recent challenges of today's nanothermometers, by continuously expanding on the important results previously obtained in the field of lanthanide-based nanothermometry, is expected to significantly contribute to the development of innovative non-toxic multimodal theranostic (combining diagnostic and therapeutic approaches) materials and devices.

References

Anderson, R. R., and J. A. Parrish. 1981. The optics of human-skin. *J. Invest. Dermatol.* 77:13–19.

Auzel, F. 2004. Upconversion and anti-Stokes processes with f and d ions in solids. *Chem. Rev.* 104:139–73.

Barnes, N. P. 2004. Lanthanide series lasers—Near infrared. In *Handbook of Laser Technology and Applications: Laser Design and Laser Systems*, edited by C. E. Webb, and J. D. C. Jones, 383–410. Boca Raton: CRC Press.

Bhaumik, J., A. K. Mittal, A. Banerjee, Y. Chisti, and U. C. Banerjee. 2015. Applications of phototheranostic nanoagents in photodynamic therapy. *Nano Res.* 8:1373–94.

Blasse, G, and B. C. Grabmaier. 1994. *Luminescent Materials*. Berlin, Heidelberg: Springer-Verlag.

Brites, C. D., P. P. Lima, N. J. Silva et al. 2012. Thermometry at the nanoscale. *Nanoscale* 4:4799–829.

Brites, C. D. S., P. P. Lima, N. J. O. Silva et al. 2011. Lanthanide-based luminescent molecular thermometers. *New J. Chem.* 35:1177–83.

Cao, B. S., Y. Y. He, Z. Q. Feng, Y. S. Li, and B. Dong. 2011. Optical temperature sensing behavior of enhanced green upconversion emissions from Er-Mo:$Yb_2Ti_2O_7$ nanophosphor. *Sens. Actuators B* 159:8–11.

Carrasco, E., B. del Rosal, F. Sanz-Rodriguez et al. 2015. Intratumoral thermal reading during photo-thermal therapy by multifunctional fluorescent nanoparticles. *Adv. Funct. Mater.* 25:615–26.

Ceron, E. N., D. H. Ortgies, B. del Rosal et al. 2015. Hybrid nanostructures for high-sensitivity luminescence nanothermometry in the second biological window. *Adv. Mater.* 27:4781–87.

Chen, D. Q., Z. Y. Wan, Y. Zhou et al. 2015. Bulk glass ceramics containing Yb^{3+}/Er^{3+}:beta-$NaGdF_4$ nanocrystals: Phase-separation-controlled crystallization, optical spectroscopy and upconverted temperature sensing behavior. *J. Alloy. Compd.* 638:21–28.

Chen, R., V. D. Ta, F. Xiao, Q. Zhang, and H. Sun. 2013. Multicolor hybrid upconversion nanoparticles and their improved performance as luminescence temperature sensors due to energy transfer. *Small* 9:1052–57.

Cheng, L., C. Wang, L. Z. Feng, K. Yang, and Z. Liu. 2014. Functional nanomaterials for phototherapies of cancer. *Chem. Rev.* 114:10869–939.

Chouahda, Z., J. P. Jouart, T. Duvaut, and M. Diaf. 2009. The use of the green emission in Er^{3+}-doped CaF_2 crystals for thermometry application. *J. Phys.: Condens. Mat.* 21:5.

Cubeddu, R., D. Comelli, C. D'Andrea, P. Taroni, and G. Valentini. 2002. Time-resolved fluorescence imaging in biology and medicine. *J. Phys. D* 35:R61–R76.

Debasu, M. L., D. Ananias, I. Pastoriza-Santos et al. 2013. All-in-one optical heater-thermometer nanoplatform operative from 300 to 2000 K based on Er^{3+} emission and blackbody radiation. *Adv. Mater.* 25:4868–74.

Diao, S., G. Hong, A. L. Antaris et al. 2015. Biological imaging without autofluorescence in the second near-infrared window. *Nano Res.* 8:3027–34.

Dieke, G. H. 1968. *Spectra and Energy Levels of Rare Earth Ions in Crystals*. New York: Interscience Publishers.

Dong, B., B. Cao, Y. He et al. 2012. Temperature sensing and *in vivo* imaging by molybdenum sensitized visible upconversion luminescence of rare-earth oxides. *Adv. Mater.* 24:1987–93.

Dong, B., R. N. Hua, B. S. Cao et al. 2014. Size dependence of the upconverted luminescence of $NaYF_4$:Er,Yb microspheres for use in ratiometric thermometry. *Phys. Chem. Chem. Phys.* 16:20009–12.

Dong, N. N., M. Pedroni, F. Piccinelli et al. 2011. NIR-to-NIR two-photon excited CaF_2: Tm^{3+},Yb^{3+} nanoparticles: Multifunctional nanoprobes for highly penetrating fluorescence bio-imaging. *ACS Nano* 5:8665–71.

dos Santos, P. V., M. T. de Araujo, A. S. Gouveia-Neto, J. A. M. Neto, and A. S. B. Sombra. 1999. Optical thermometry through infrared excited upconversion fluorescence emission in Er^{3+}- and Er^{3+}-Yb^{3+}-doped chalcogenide glasses. *IEEE J. Quantum Electron.* 35:395–99.

Du, P., L. H. Luo, and J. S. Yu. 2015a. Low-temperature thermometry based on upconversion emission of Ho/Yb-codoped $Ba_{0.77}Ca_{0.23}TiO_3$ ceramics. *J. Alloy. Compd.* 632:73–77.

Du, P., L. H. Luo, Q. Y. Yue, and W. P. Li. 2015b. The simultaneous realization of high- and low-temperature thermometry in Er^{3+}/Yb^{3+}-codoped Y_2O_3 nanoparticles. *Mater. Lett.* 143:209–11.

Du, P. and J. S. Yu. 2015. Effect of molybdenum on upconversion emission and temperature-sensing properties in $Na_{0.5}Bi_{0.5}TiO_3$:Er/Yb ceramics. *Ceram. Int.* 41:6710–14.

Gavrilovic, T. V., D. J. Jovanovic, V. Lojpur, and M. D. Dramicanin. 2014. Multifunctional Eu^{3+}- and Er^{3+}/Yb^{3+}-doped $GdVO_4$ nanoparticles synthesized by reverse micelle method. *Sci. Rep.* 4:9.

Hemmer, E., A. Benayas, F. Légaré, and F. Vetrone. 2016. Exploiting the biological windows: Current perspectives on fluorescent bioprobes emitting above 1000 nm. *Nanoscale Horiz.* 1:168–84.

Hemmer, E., M. Quintanilla, F. Légaré, and F. Vetrone. 2015. Temperature-induced energy transfer in dye-conjugated upconverting nanoparticles: A new candidate for nanothermometry. *Chem. Mater.* 27:235–44.

Hemmer, E., N. Venkatachalam, H. Hyodo et al. 2013a. Upconverting and NIR emitting rare earth based nanostructures for NIR-bioimaging. *Nanoscale* 5:11339–61.

Hemmer, E., F. Vetrone, and K. Soga. 2014. Lanthanide-based nanostructures for optical bioimaging: Small particles with large promise. *MRS Bull.* 39:960–64.

Hemmer, E., T. Yamano, H. Kishimoto et al. 2013b. Cytotoxic aspects of gadolinium oxide nanostructures for up-conversion and NIR bioimaging. *Acta Biomater.* 9:4734–43.

Huang, F., Y. Gao, J. C. Zhou, J. Xua, and Y. S. Wang. 2015. Yb^{3+}/Er^{3+} co-doped $CaMoO_4$: A promising green upconversion phosphor for optical temperature sensing. *J. Alloy. Compd.* 639:325–29.

Huang, J. C., B. Z. He, Z. H. Cheng, and L. Zhou. 2015. Upconverting PAAm/PNIPAM/$NaYF_4$:Yb:Er hydrogel with enhanced luminescence temperature sensitivity. *J. Lumin.* 160:254–57.

Huang, Y., F. Rosei, and F. Vetrone. 2015. A single multifunctional nanoplatform based on upconversion luminescence and gold nanorods. *Nanoscale* 7:5178–85.

Idris, N. M., M. K. G. Jayakumar, A. Bansal, and Y. Zhang. 2015. Upconversion nanoparticles as versatile light nanotransducers for photoactivation applications. *Chem. Soc. Rev.* 44:1449–78.

Jaque, D., L. M. Maestro, E. Escudero et al. 2013. Fluorescent nano-particles for multiphoton thermal sensing. *J. Lumin.* 133:249–53.

Jaque, D., L. Martinez Maestro, B. del Rosal et al. 2014a. Nanoparticles for photothermal therapies. *Nanoscale* 6:9494–530.

Jaque, D., B. del Rosal, E. M. Rodriguez et al. 2014b. Fluorescent nanothermometers for intracellular thermal sensing. *Nanomedicine* 9:1047–62.

Jaque, D. and F. Vetrone. 2012. Luminescence nanothermometry. *Nanoscale* 4:4301–26.

Jiang, S., P. Zeng, L. Q. Liao et al. 2014. Optical thermometry based on upconverted luminescence in transparent glass ceramics containing $NaYF_4$:Yb^{3+}/Er^{3+} nanocrystals. *J. Alloy. Compd.* 617:538–41.

Ju, Q., D. Tu, Y. Liu et al. 2012. Amine-functionalized lanthanide-doped $KGdF_4$ nanocrystals as potential optical/magnetic multimodal bioprobes. *J. Am. Chem. Soc.* 134:1323–30.

Klier, D. T. and M. U. Kumke. 2015a. Upconversion luminescence properties of $NaYF_4$:Yb:Er nanoparticles codoped with Gd^{3+}. *J. Physi. Chem. C* 119:3363–73.

Klier, D. T. and M. U. Kumke. 2015b. Upconversion $NaYF_4$:Yb:Er nanoparticles co-doped with Gd^{3+} and Nd^{3+} for thermometry on the nanoscale. *RSC Adv.* 5:67149–56.

Klimov, N. N., S. Mittal, M. Berger, and Z. Ahmed. 2015. On-chip silicon waveguide Bragg grating photonic temperature sensor. *Opt. Lett.* 40:3934–36.

Lai, B. Y., L. Feng, J. Wang, and Q. A. Su. 2010. Optical transition and upconversion luminescence in Er^{3+} doped and Er^{3+}-Yb^{3+} co-doped fluorophosphate glasses. *Opt. Mater.* 32:1154–60.

Lakowicz, J. R., H. Szmacinski, K. Nowaczyk, K. W. Berndt, and M. Johnson. 1992. Fluorescence lifetime imaging. *Anal. Biochem.* 202:316–30.

Lee, D. E., H. Koo, I. C. Sun et al. 2012. Multifunctional nanoparticles for multimodal imaging and theragnosis. *Chem. Soc. Rev.* 41:2656–72.

Li, D. D., Q. Y. Shao, Y. Dong, and J. Q. Jiang. 2014. Temperature sensitivity and stability of $NaYF_4$:Yb^{3+}, Er^{3+} core-only and core–shell upconversion nanoparticles. *J. Alloy. Compd.* 617:1–6.

Li, T., C. F. Guo, S. S. Zhou, C. K. Duan, and M. Yin. 2015. Highly sensitive optical thermometry of Yb^{3+}-Er^{3+} codoped $AgLa(MoO_4)_2$ green upconversion phosphor. *J. Am. Ceram. Soc.* 98:2812–16.

Liu, G. F., L. L. Fu, Z. Y. Gao et al. 2015. Investigation into the temperature sensing behavior of Yb^{3+} sensitized Er^{3+} doped Y_2O_3, YAG and $LaAlO_3$ phosphors. *RSC Adv.* 5:51820–27.

Liu, L., Y. J. Chen, X. L. Zhang, Z. G. Zhang, and Y. X. Wang. 2013. Improved optical thermometry in Er^{3+}:Y_2O_3 nanocrystals by re-calcination. *Opt. Commun.* 309:90–94.

Liu, L., Y. X. Wang, X. R. Zhang et al. 2011. Optical thermometry through green and red upconversion emissions in Er^{3+}/Yb^{3+}/Li^{+}:ZrO_2 nanocrystals. *Opt. Commun.* 284:1876–79.

Liu, Y. S., D. T. Tu, H. M. Zhu, E. Ma, and X. Y. Chen. 2013. Lanthanide-doped luminescent nano-bioprobes: From fundamentals to biodetection. *Nanoscale* 5:1369–84.

Lojpur, V., M. Nikolic, L. Mancic, O. Milosevic, and M. D. Dramicanin. 2013. Y_2O_3:Yb,Tm and Y_2O_3:Yb,Ho powders for low-temperature thermometry based on up-conversion fluorescence. *Ceram. Int.* 39:1129–34.

Maciel, G. S., M. Alencar, C. B. de Araujo, and A. Patra. 2010. Upconversion emission of $BaTiO_3$:Er^{3+} nanocrystals: Influence of temperature and surrounding medium. *J. Nanosci. Nanotechnol.* 10:2143–48.

Mahata, M. K., K. Kumar, and V. K. Rai. 2015. Er^{3+}-Yb^{3+} doped vanadate nanocrystals: A highly sensitive thermographic phosphor and its optical nanoheater behavior. *Sens. Actuators B* 209:775–80.

Marciniak, L., A. Bednarkiewicz, M. Stefanski et al. 2015. Near infrared absorbing near infrared emitting highly-sensitive luminescent nanothermometer based on Nd^{3+} to Yb^{3+} energy transfer. *Phys. Chem. Chem. Phys.* 17:24315–21.

Mecklenburg, M., W. A. Hubbard, E. R. White et al. 2015. Nanoscale temperature mapping in operating microelectronic devices. *Science* 347:629–32.

Mednitz, I. and N. Hildebrandt. 2014. *FRET––Förster Resonance Energy Transfer, from Theory to Applications*. Weinheim, Germany: Wiley-VCH.

Melamed, J. R., R. S. Edelstein, and E. S. Day. 2015. Elucidating the fundamental mechanisms of cell death triggered by photothermal therapy. *ACS Nano* 9:6–11.

Pandey, A. and V. K. Rai. 2013. Optical thermometry using FIR of two close lying levels of different ions in Y_2O_3:Ho^{3+}-Tm^{3+}-Yb^{3+} phosphor. *Appl. Phys. B* 113:221–25.

Pandey, A., V. K. Rai, V. Kumar, V. Kumar, and H. C. Swart. 2015. Upconversion based temperature sensing ability of Er^{3+}-Yb^{3+} codoped $SrWO_4$: An optical heating phosphor. *Sens. Actuators B* 209:352–58.

Pandey, A., S. Som, V. Kumar et al. 2014. Enhanced upconversion and temperature sensing study of Er^{3+}-Yb^{3+} codoped tungsten-tellurite glass. *Sens. Actuators B* 202:1305–12.

Peng, D. F., X. S. Wang, C. N. Xu et al. 2012. Bright upconversion luminescence and increased Tc in $CaBi_2Ta_2O_9$:Er high temperature piezoelectric ceramics. *J. Appl. Phys.* 111:5.

Pereira, A. F., K. U. Kumar, W. F. Silva et al. 2015. Yb^{3+}/Tm^{3+} co-doped $NaNbO_3$ nanocrystals as three-photon-excited luminescent nanothermometers. *Sens. Actuators B* 213:65–71.

Perpiñà, X., M. Vellvehi, and X. Jordà 2016. Thermal issues in microelectronics. In *Thermometry at the Nanoscale: Techniques and Selected Applications*, edited by. L. D. Carlos, and F. Palacio, 383–436. Cambridge: The Royal Society of Chemistry.

Prodi, L., E. Rampazzo, F. Rastrelli, A. Speghini, and N. Zaccheroni. 2015. Imaging agents based on lanthanide doped nanoparticles. *Chem. Soc. Rev.* 44:4922–52.

Quintanilla, M., A. Benayas, R. Naccache, and F. Vetrone. 2016. Luminescent nanothermometry with lanthanide-doped nanoparticles. In *Thermometry at the Nanoscale: Techniques and Selected Applications*, edited by L. D. Carlos, and F. Palacio, 124–66. Cambridge: The Royal Society of Chemistry.

Quintanilla, M., I. X. Cantarelli, M. Pedroni, A. Speghini, and F. Vetrone. 2015. Intense ultraviolet upconversion in water dispersible SrF_2: Tm^{3+}, Yb^{3+} nanoparticles: The effect of the environment on light emissions. *J. Mater. Chem. C* 3:3108–13.

Quintanilla, M., E. Cantelar, F. Cussó, M. Villegas, and A. C. Caballero. 2011. Temperature sensing with up-converting submicron-sized $LiNbO_3$:Er^{3+}/Yb^{3+} particles. *Appl. Phys. Express* 4:022601.

Rakov, N., and G. S. Maciel. 2012. Three-photon upconversion and optical thermometry characterization of Er^{3+}:Yb^{3+} co-doped yttrium silicate powders. *Sens. Actuators B* 164:96–100.

Rocha, U., C. Jacinto, W. F. Silva et al. 2013. Subtissue thermal sensing based on neodymium-doped LaF_3 nanoparticles. *ACS Nano* 7:1188–99.

Rocha, U., K. U. Kumar, C. Jacinto et al. 2014. Nd^{3+} doped LaF_3 nanoparticles as self-monitored photo-thermal agents. *Appl. Phys. Lett.* 104:053703.

Rohani, S., M. Quintanilla, S. Tuccio et al. 2015. Enhanced luminescence, collective heating, and nanothermometry in an ensemble system composed of lanthanide-doped upconverting nanoparticles and gold nanorods. *Adv. Opt. Mater.* 3:1606–13.

Rothamer, D. A., and J. Jordan. 2012. Planar imaging thermometry in gaseous flows using upconversion excitation of thermographic phosphors. *Appl. Phys. B* 106:435–44.

Savchuk, O. A., J. J. Carvajal, M. C. Pujol et al. 2015. Ho,Yb:$KLu(WO_4)_2$ nanoparticles: A versatile material for multiple thermal sensing purposes by luminescent thermometry. *J. Phys. Chem. C* 119:18546–58.

Savchuk, O. A., P. Haro-Gonzalez, J. J. Carvajal et al. 2014. Er:Yb:NaY_2F_5O up-converting nanoparticles for sub-tissue fluorescence lifetime thermal sensing. *Nanoscale* 6:9727–33.

Sayoud, A., J. P. Jouart, N. Trannoy, M. Diaf, and T. Duvaut. 2012. Temperature measurements inside an Er^{3+}-Yb^{3+} co-doped fluoride crystal heated by a NIR laser diode and probed by red-to-green upconversion. *J. Lumin.* 132:566–69.

Schartner, E. P., and T. M. Monro. 2014. Fibre tip sensors for localised temperature sensing based on rare earth-doped glass coatings. *Sensors* 14:21693–701.

Shan, J., J. Chen, J. Meng et al. 2008. Biofunctionalization, cytotoxicity, and cell uptake of lanthanide doped hydrophobically ligated $NaYF_4$ upconversion nanophosphors. *J. Appl. Phys.* 104:094308.

Shanmugam, V., S. Selvakumar, and C. S. Yeh. 2014. Near-infrared light-responsive nanomaterials in cancer therapeutics. *Chem. Soc. Rev.* 43:6254–87.

Singh, A. K. 2007. Ho^{3+}:TeO_2 glass, a probe for temperature measurements. *Sens. Actuators A*136:173–77.

Singh, A. K., P. K. Shahi, S. B. Rai, and B. Ullrich. 2015. Host matrix impact on Er^{3+} upconversion emission and its temperature dependence. *RSC Adv.* 5:16067–73.

Singh, S. K., K. Kumar, and S. B. Rai. 2009. Er^{3+}/Yb^{3+} codoped Gd_2O_3 nano-phosphor for optical thermometry. *Sens. Actuators A* 149:16–20.

Smith, A. M., M. C. Mancini, and S. Nie. 2009. Bioimaging: Second window for *in vivo* imaging. *Nat. Nanotechnol.* 4:710–11.

Soni, A. K., R. Dey, and V. K. Rai. 2015. Stark sublevels in Tm^{3+}-Yb^{3+} codoped $Na_2Y_2B_2O_7$ nanophosphor for multifunctional applications. *RSC Adv.* 5:34999–5009.

Sordillo, L. A., Y. Pu, S. Pratavieira, Y. Budansky, and R. R. Alfano. 2014. Deep optical imaging of tissue using the second and third near-infrared spectral windows. *J. Biomed. Opt.* 19:056004.

Verma, R. K., and S. B. Rai. 2012. Laser induced optical heating from Yb^{3+}/Ho^{3+}:$Ca_{12}Al_{14}O_{33}$ and its applicability as a thermal probe. *J. Quant. Spectrosc. Radiat. Transfer* 113:1594–600.

Vetrone, F., R. Naccache, V. Mahalingam, C. G. Morgan, and J. A. Capobianco. 2009. The active-core/active-shell approach: A strategy to enhance the upconversion luminescence in lanthanide-doped nanoparticles. *Adv. Funct. Mater.* 19:2924–29.

Vetrone, F., R. Naccache, A. Zamarron et al. 2010. Temperature sensing using fluorescent nanothermometers. *ACS Nano* 4:3254–58.

Wang, G. F., Q. Peng, and Y. D. Li. 2011. Lanthanide-doped nanocrystals: Synthesis, optical-magnetic properties, and applications. *Accounts Chem. Res.* 44:322–32.

Wang, R., X. L. Zhang, F. Liu, Y. J. Chen, and L. Liu. 2015. Concentration effects on the FIR technique for temperature sensing. *Opt. Mater.* 43:18–24.

Wang, S. P., S. Westcott, and W. Chen. 2002. Nanoparticle luminescence thermometry. *J. Phys. Chem. B* 106:11203–09.

Wang, X. D., O. S. Wolfbeis, and R. J. Meier. 2013. Luminescent probes and sensors for temperature. *Chem. Soc. Rev.* 42:7834–69.

Wang, X., X. G. Kong, Y. Yu, Y. J. Sun, and H. Zhang. 2007. Effect of annealing on upconversion luminescence of ZnO:Er^{3+} nanocrystals and high thermal sensitivity. *J. Phys. Chem. C* 111:15119–24.

Wang, X., Q. Liu, Y. Bu et al. 2015. Optical temperature sensing of rare-earth ion doped phosphors. *RSC Adv.* 5:86219–36.

Wawrzynczyk, D., A. Bednarkiewicz, M. Nyk, W. Strek, and M. Samoc. 2012. Neodymium(III) doped fluoride nanoparticles as non-contact optical temperature sensors. *Nanoscale* 4:6959–61.

Wegh, R. T., A. Meijerink, R. J. Lamminmaki, and J. Holsa. 2000. Extending Dieke's diagram. *J. Lumin.* 87–89:1002–04.

Xing, L. L., Y. L. Xu, R. Wang, W. Xu, and Z. G. Zhang. 2014. Highly sensitive optical thermometry based on upconversion emissions in Tm^{3+}/Yb^{3+} codoped $LiNbO_3$ single crystal. *Opt. Lett.* 39:454–57.

Xu, W., X. Y. Gao, L. J. Zheng, Z. G. Zhang, and W. W. Cao. 2012a. Short-wavelength upconversion emissions in Ho^{3+}/Yb^{3+} codoped glass ceramic and the optical thermometry behavior. *Opt. Express* 20:18127–37.

Xu, W., Q. T. Song, L. J. Zheng, Z. G. Zhang, and W. W. Cao. 2014. Optical temperature sensing based on the near-infrared emissions from Nd^{3+}/Yb^{3+} codoped $CaWO_4$. *Opt. Lett.* 39:4635–38.

Xu, W., Z. G. Zhang, and W. W. Cao. 2012b. Excellent optical thermometry based on short-wavelength upconversion emissions in Er^{3+}/Yb^{3+} codoped $CaWO_4$. *Opt. Lett.* 37:4865–67.

Xu, W., H. Zhao, Y. X. Li et al. 2013a. Optical temperature sensing through the upconversion luminescence from Ho^{3+}/Yb^{3+} codoped $CaWO_4$. *Sens. Actuators B* 188:1096–100.

Xu, W., H. Zhao, Z. G. Zhang, and W. W. Cao. 2013b. Highly sensitive optical thermometry through thermally enhanced near infrared emissions from Nd^{3+}/Yb^{3+} codoped oxyfluoride glass ceramic. *Sens. Actuators B* 178:520–24.

Yang, W. F., X. Y. Li, D. Z. Chi, H. J. Zhang, and X. G. Liu. 2014. Lanthanide-doped upconversion materials: Emerging applications for photovoltaics and photocatalysis. *Nanotechnology* 25:16.

Yang, X. X., Z. L. Fu, Y. M. Yang et al. 2015. Optical temperature sensing behavior of high-efficiency upconversion: Er^{3+}-Yb^{3+} co-doped $NaY(MoO_4)_2$ phosphor. *J. Am. Ceram. Soc.* 98:2595–600.

Yang, Y. M., C. Mi, F. Y. Jiao et al. 2014. A novel multifunctional upconversion phosphor: Yb^{3+}/Er^{3+} codoped La_2S_3. *J. Am. Ceram. Soc.* 97:1769–75.

Yang, Y., C. Mi, F. Yu et al. 2014. Optical thermometry based on the upconversion fluorescence from Yb^{3+}/Er^{3+} codoped La_2O_2S phosphor. *Ceram. Int.* 40:9875–80.

Yao, J., M. Yang, and Y. X. Duan. 2014. Chemistry, biology, and medicine of fluorescent nanomaterials and related systems: New insights into biosensing, bioimaging, genomics, diagnostics, and therapy. *Chem. Rev.* 114:6130–78.

Zagumennyi, A. I., V. A. Mikhailov, and I. A. Shcherbakov. 2004. Rare earth ion lasers—Nd^{3+}. In *Handbook of Laser Technology and Applications: Laser Design and Laser Systems*, edited by C. E. Webb, and J. D. C. Jones, 353–82. Boca Raton: CRC Press.

Zhang, J. P., F. Y. Liu, T. Li, X. X. He, and Z. X. Wang. 2015. Surface charge effect on the cellular interaction and cytotoxicity of $NaYF_4$:Yb^{3+}, Er^{3+}@SiO_2 nanoparticles. *RSC Adv.* 5:7773–80.

Zheng, K. Z., Z. Y. Liu, C. J. Lv, and W. P. Qin. 2013. Temperature sensor based on the UV upconversion luminescence of Gd^{3+} in Yb^{3+}-Tm^{3+}-Gd^{3+} codoped $NaLuF_4$ microcrystals. *J. Mater. Chem. C* 1:5502–07.

Zheng, K. Z., W. Y. Song, G. H. He, Z. Yuan, and W. P. Qin. 2015. Five-photon UV upconversion emissions of Er^{3+} for temperature sensing. *Opt. Express* 23:7653–58.

Zheng, S. H., W. B. Chen, D. Z. Tan et al. 2014. Lanthanide-doped $NaGdF_4$ core–shell nanoparticles for non-contact self-referencing temperature sensors. *Nanoscale* 6:5675–79.

Zhou, H., M. Sharma, O. Berezin, D. Zuckerman, and M. Y. Berezin. 2016. Nanothermometry: From microscopy to thermal treatments. *Chem. Phys. Chem.* 17:27–36.

Zhou, S. S., G. C. Jiang, X. Y. Li et al. 2014a. Strategy for thermometry via Tm^{3+}-doped $NaYF_4$ core–shell nanoparticles. *Opt. Lett.* 39:6687–90.

Zhou, S. S., G. C. Jiang, X. T. Wei et al. 2014b. Pr^{3+}-doped beta-$NaYF_4$ for temperature sensing with fluorescence intensity ratio technique. *J. Nanosci. Nanotechnol.* 14:3739–42.

Zhou, S. S., S. Jiang, X. T. Wei et al. 2014c. Optical thermometry based on upconversion luminescence in Yb^{3+}/Ho^{3+} co-doped $NaLuF_4$. *J. Alloy. Compd.* 588:654–57.

Zou, H., X. S. Wang, Y. F. Hu et al. 2015. Optical thermometry based on the upconversion luminescence from Er doped $Bi_7Ti_4TaO_{21}$ ferroelectric ceramics. *J. Mater. Sci.: Mater. Electr.* 26:6502–05.

Taylor & Francis
Taylor & Francis Group
http://taylorandfrancis.com